Controlling Particle Morphologies at Fluid Interfaces: Macro- and Micro- approaches

Shilpa Naidu Beesabathuni

A dissertation
submitted in partial fulfillment of the
requirements for the degree of

Doctor of Philosophy

University of Washington
2014

Reading Committee:
Amy Shen Fried
Jae-Hyun Chung
George Homsy

Program Authorized to Offer Degree:
Mechanical Engineering

University of Washington

Abstract

Controlling Particle Morphologies at Fluid Interfaces: Macro- and Micro- approaches

Shilpa Naidu Beesabathuni

Chair of the Supervisory Committee:
Associate Professor Amy Shen Fried
Department of Mechanical Engineering

The controlled generation of varying shaped particles is important for many applications: consumer goods, biomedical diagnostics, food processing, adsorbents and pharmaceuticals which can benefit from the availability of geometrically complex and chemically inhomogeneous particles. This thesis presents two approaches to spherical and non-spherical particle synthesis using macro and microfluidics.

In the first approach, a droplet microfluidic technique is explored to fabricate spherical conducting polymer, polyaniline, particles with precise control over morphology and functionality. Microfluidics has recently emerged as an important

alternate to the synthesis of complex particles. The conducting polymer, polyaniline, is widely used and known for its stability, high conductivity, and favorable redox properties. In this approach, monodisperse micron-sized polyaniline spherical particles were synthesized using two-phase droplet microfluidics from Aniline and Ammonium persulfate oxidative polymerization in an oil-based continuous phase. The morphology of the polymerized particles is porous in nature which can be used for encapsulation as well as controlled release applications. Encapsulation of an enzyme, glucose oxidase, was also performed using the technique to synthesize microspheres for glucose sensing. The polymer microspheres were characterized using SEM, UV-Vis and EDX to understand the relationship between their microstructure and stability.

In the second approach, molten drop impact in a cooling aqueous medium to generate non-spherical particles was explored. Viscoelastic wax based materials are widely used in many applications and their performance and application depends on the particle morphology and size. The deformation of millimeter size molten wax drops as they impacted an immiscible liquid interface was investigated. Spherical molten wax drops impinged on a cooling water bath, then deformed and as a result of solidification

were arrested into various shapes such as *ellipsoids, mushrooms, spherulites* and *discs*. The final morphology of the wax particles is governed by the interfacial, inertial, viscous and thermal effects, which can be studied over a range of Weber, Capillary, Reynolds and Stefan numbers. A simplified Stefan problem for a spherical drop was solved. The time required to initiate a phase transition at the interface of the molten wax and water after impact was estimated and correlated with the drop deformation history and final wax particle shape to develop a capability to predict the shape.

While the microfluidic synthesis approach offers precise control over morphology and functionality, large particle throughput is a limitation. The drop impact in a liquid medium emulsion approach is limited to crosslinking or heat sensitive materials but can be extended to large scale production for industrial applications. Both approaches are simple, robust and cost effective making them viable and attractive solutions for complex particle synthesis. The choice of the approach is dependent on considerations such as particle material, size, shape, throughput and end application.

Table of Contents

List of Figures

Page

List of Tables

Page

Acknowledgements

I would like to thank my committee chair and adviser, Amy Shen, for guidance and support. She was instrumental in molding a naive student to adopt a greater understanding of science. She is a mentor and friend and I will cherish the lessons learnt from her. I am very happy to have worked with Prof. Bud Homsy who was very patient with me and helped me develop a deeper understanding of science within the very few meetings that we've had. Thanks to Prof. Jae-Hyun Chung for guiding me on a large part of my research. Thanks to Mr. Seth Lindberg, Mr. Chris Wesner and Dr. Marco Caggioni (Procter & Gamble) for fruitful discussions during the course of our exciting collaboration.

I would like to thank my committee members Prof. René Overney, Prof. Guozhong Cao and Prof. Jiangyu Li for their support and fresh perspectives.

This work was supported by NSF (CBET-CAREER 0852471), University of Washington Royalty Research Fund 65-5738 and Procter & Gamble. Part of this work was carried out at the Nanotech User Facility, Microfabrication Facility, Mass Spectrometry Facility, Material Science User Facility and the Nanomanufacturing Lab at the University of Washington.

This section will not be complete without the mention of some wonderful people who have made this journey fun. A big shout out to my lab group with whom I have spent a better part of the past 3.5 years; Wanwisa and Maria who have been very warm and extremely helpful. Thanks to my amazing friends (too many to name) who have

become my extended family and have been supportive as well as very critical. Finally, my journey so far would have been impossible without the encouragement of my family. They have taught me to dream big and to go after it.

Chapter 1
Introduction

1.1 Motivation

Soft matter and polymeric systems, in which the macroscopic properties have significant dependency on their microscopic structures, can encompass a wide range of substances including polymers, gels, surfactants, liquid crystals, micelles (clumps of polar molecules), and microemulsions. All of these share the same basic characteristics – weak interactions between structural units and large numbers of ways to arrange themselves internally. The physical and chemical properties of soft matter are increasingly important in a wide range of applications. Research studies are increasingly motivated by the commercial significance of products that have complex components. They find industrial applications in consumer goods, pharmaceuticals, biofuels, solar cells, lubricants, oil recovery, plastics, liquid crystals, paints and in the field of biological and biomedical sciences (biochemical lab on chip systems, biosensors, separation devices and drug delivery systems). Perhaps the most fascinating aspect of soft matter science lies in the fact that the physical systems considered are not atomic or molecular in nature: the constituent particles of what are synonymously known as *complex fluids* can be macromolecular aggregates whose spatial extent lies in the domain between 1 nm and 1 μm. Although there is an abundance of naturally occurring soft matter systems, a large variety of complex fluids are man-made. Over the last few decades, there has been notable research, experimentally and

theoretically, in manipulating soft matter and fabricating regular and monodispersed particles. Several fabrication techniques have been designed to generate particles with control over shape, size and functionality. The shape and size of the particles is of prime importance in governing the macro and microscopic properties.

A popular way to fabricate particles is the use of emulsification techniques. An emulsion is a mixture of two immiscible liquids, one of which is dispersed in the continuous phase of the other. Common emulsions include oil-in-water (O/W) and water-in-oil (W/O). Technological applications of emulsions range from drug delivery and polymerization processing to oil recover and hazardous material handling. Of particular interest are recent advances in the production of ordered materials with novel optical and mechanical properties by way of emulsion templating, emulsion polymerization or thermal effects in emulsions [1, 2].

This thesis explores the fabrication approach of various particle shapes using drop emulsion techniques. Each fabrication technique discussed below has its own unique set of advantages and limitations. Particle shapes can be classified as spherical and non-spherical. For fabricating non-spherical particles, spherical droplets can be used as starting materials and then manipulated into different morphologies. The critical design considerations of particles are highly dependent on the applications. Among the considerations are the size, size distribution, shape, mass transport properties and the rheological properties of the material.

1.2 Particle Fabrication

Several methods for producing particles are used today. These methods can be classified into two main groups: (i) *ab initio* synthesis of particles and (ii) manipulation of previously fabricated spherical droplets into non-spherical geometries. Often the *ab initio* synthesis routes are more difficult but produce a broader range of shapes. Manipulation techniques, on the other hand, can be simpler and low cost but usually cannot produce as diverse a range of shapes.

In the first category, fabrication techniques on a large scale in the industry include high pressure homogenizers, ultrasound homogenizers, and rotor-stator systems [3, 4]. These instruments apply a high shear stress to deform and disrupt large droplets into smaller ones. The prepared emulsions are polydispersed which makes them intrinsically unstable. On a smaller scale, techniques such as lithography, microfluidics and photopolymerization, often in combination, can be used to synthesize spherical and subsequently non-spherical particles [5-8]. In the second category, spherical droplets are used as starting materials and manipulated into different morphologies. Self-assembly is one of the techniques that can fabricate a wide size range of particles in micro- to nanoscale. However, it relies on shape formation through controlled self-assembly and cannot be engineered as precisely as in the case of other methods [9]. Extrusion combined with emulsification, on the other hand, offers more freedom in controlling the morphologies.

Two techniques belonging to each of the above categories have emerged in the recent decades to manipulate the shapes of particles – (i) droplet microfluidics and (ii) drop impact on a liquid substrate. Spherical and non-spherical particles can be fabricated using the above two techniques individually or together. This thesis will explore the above two techniques in detail.

1.2.1 Droplet Microfluidics

Microfluidics has recently emerged as an important alternative route to the synthesis of such complex particles. Since the advent of microfluidics approximately two decades ago, there has been a steady increase in the interest and development of tools for fluid flow at the microscale [10]. This multidisciplinary technology involves fundamental concepts from a broad range of fields from biology to electrical engineering. This field generates an equally diverse array of applications that varies from drug delivery to point-of-care diagnostic chips to organic synthesis [11] and microreactors [12-14]. Microfluidic technology holds great promise as it can perform typical laboratory operations using a fraction of the volume of reagents in significantly less time. Reagents can be significantly reduced from milliliters and microliters to nanoliters and femtoliters whereas hours of reaction time could be decreased to mere seconds or less.

One subcategory of microfluidics is droplet-based microfluidics [15, 16]. Unlike continuous flow systems, droplet-based systems constrained in microchannels focus on creating discrete volumes of emulsions with the use of immiscible phases. Microfluidic systems are characterized by the low-Reynolds number flow regime which dictates that all fluid flow is essentially laminar. Continuous-flow based systems have exploited this phenomenon to create many novel micro-environments [17]. For instance, a simple device has been created to fabricate Janus particles with two or more distinct physical properties [18]. Laminar flow behavior also allows for the generation of precise concentration gradients that have been employed in the study of cell migration [19]. Although continuous flow devices offer fine control over flow characteristics, scaling up is a challenge as the size of devices scales almost linearly with the number of parallel experiments. Droplet microfluidics, however, has the ability to perform a large number of

reactions without increasing device size or complexity. In addition, recent discoveries have demonstrated that droplet microfluidic systems can perform simple Boolean logic functions, a critical step towards the realization of a microfluidic computer chip [20-22].

Droplet-based microfluidics involves the generation and manipulation of discrete droplets inside microdevices [23, 24]. Droplet microfluidics usually exploits three common designs for monodisperse drop formation: those based on flow focusing phenomenon, those based on co-flowing phenomenon and those relying on the shearing of one fluid by another immiscible fluid (i.e., T-shaped channel), as shown in Figure 1.1 [25]. This method produces highly monodisperse droplets in the nanometer to micrometer diameter range, at rates of up to twenty thousand per second [26]. Due to high surface area to volume ratios at the microscale, heat and mass transfer times and diffusion distances are shorter, facilitating faster reaction times. Unlike in continuous-flow systems, droplet-based microfluidics allows for independent control of each droplet, thus generating microreactors that can be individually transported, mixed, and analyzed [27, 28]. Since multiple identical microreactor units can be formed in a short time, parallel processing and experimentation can easily be achieved, allowing large data sets to be acquired efficiently. Droplet microfluidics also offers greater potential for increased throughput and scalability than continuous-flow systems. In the past 5 years, several groups have used droplet microfluidics to form irregular particles [29], double emulsions [30], hollow microcapsules [31], and microbubbles [32]. These particles can be used in a diverse range of applications, including the synthesis of biomolecules, drug delivery, and diagnostic testing.

In this thesis, droplet microfluidics is utilized to fabricate conductive polymer microspheres.

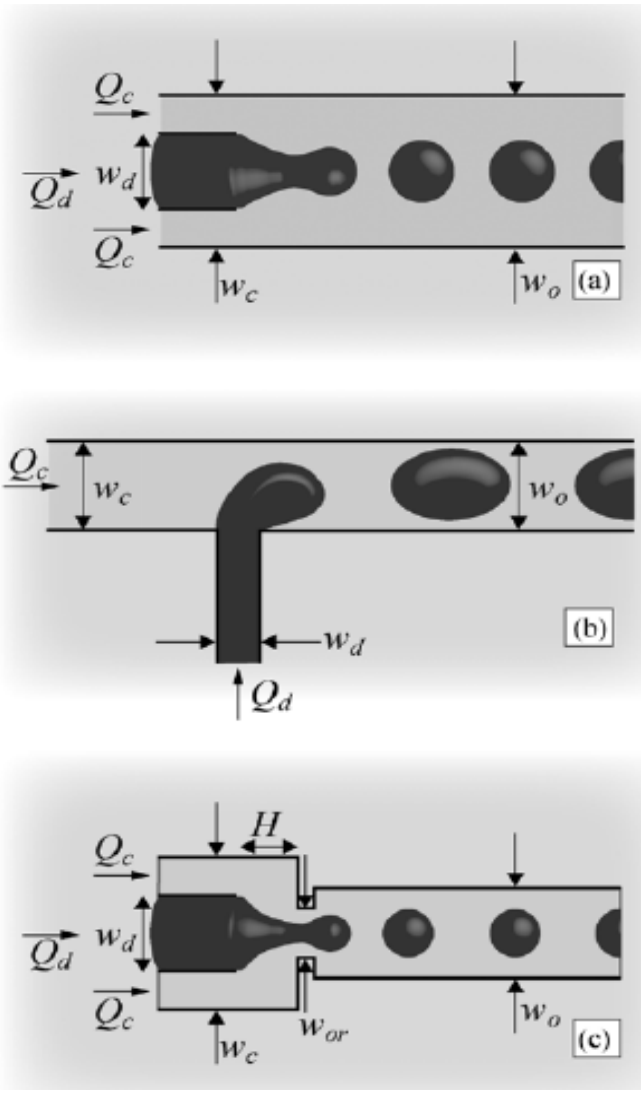

Figure 1.1. Schematic examples of (a) co-flowing (b) T-junction and (c) flow-focusing devices detailing important dimensions (Reproduced with permission from Christopher and Anna, 2007).

1.2.2 Drop Impact at a Liquid Interface

Starting with spherical drops of the material, which can be generated either by extrusion at the millimeter scale or droplet microfluidics at the micron scale, chemical or thermal effects can be applied in a bulk medium to crosslink or solidify the material. Recent research has reported non-

spherical particle fabrication by impinging and deforming microgel drops in a crosslinking bulk medium [33, 34]. Liquid drops extruded and impinged upon a liquid pool can give rise to a wide variety of shapes. Studies of drop impact are commonly motivated by its ubiquity in nature and industry. Liquid drop impact and subsequent deformation is also of fundamental importance due to its application in a wealth of areas including inkjet printing, food processing, spray coating, drug delivery, optical sensing, soil erosion and turbine wear [35-39]. In comparison to traditional crosslinking, polymerization, or solidification inside microchannels in droplet microfluidics, drop impact in a liquid medium allows the manipulation of interfacial dynamics for precise control of morphology.

Many studies have been performed on the deformation of isothermal drops upon impact with solid and liquid surfaces, which have been covered extensively in two recent reviews by Rein [40] and Yarin [41]. The result of the drop impact on a liquid interface depends on the rheological properties of the drop, the impacted surface, the fluid which the drop traverses before impact, impact velocity and geometric aspects. When a liquid drop impacts a solid substrate, the drop may deposit into a thin disc, disintegrate into secondary drops, or recede and possibly rebound and bounce [42]. The impact of a liquid drop on a liquid pool may broadly be classified into three categories – coalescence, splashing or bouncing off the surface [40-42] (Figure 1.2). The interfacial dynamics of the impact and subsequently the morphology of the drop can be controlled by manipulating the material properties of the drop and bath fluids and the geometric aspects.

In the case of coalescence the drop disappears quickly in the target liquid. A small crater is formed but otherwise the impacted surface is hardly disturbed and no secondary droplets are

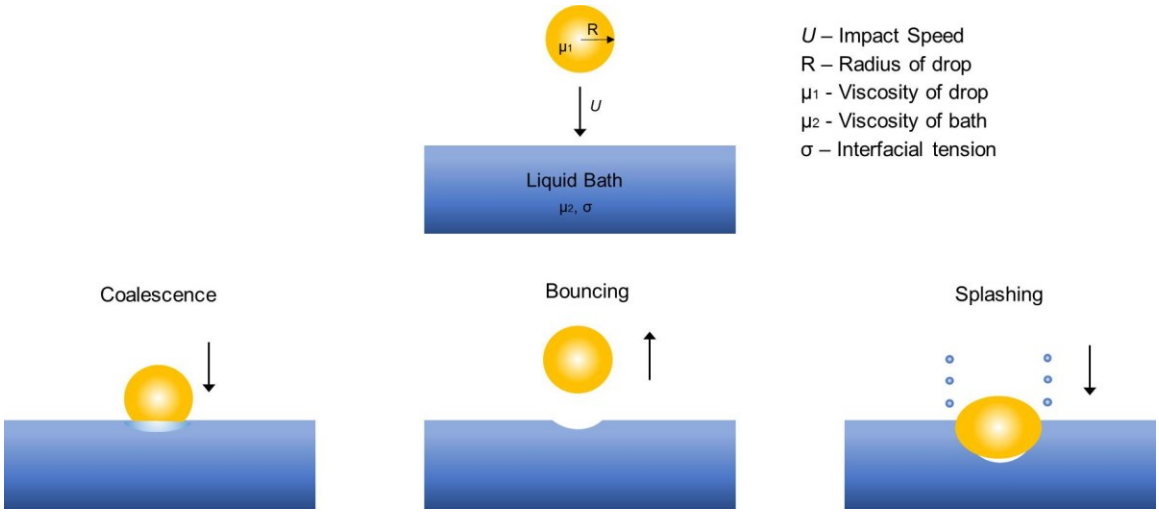

Figure 1.2. Impact of a drop on a liquid surface may result in coalescence, bouncing or splashing

The nature of the outcome is dependent on whether the fluids are miscible or immiscible. Drops impinging on the surface of a liquid miscible with it can entrain air bubbles and eventually coalesce with the target pool [51-54]. Drops impinging on immiscible liquids can form lens-shaped structure or retain a metastable spherical configuration above the free surface of the liquid [55, 56].

produced. This event is usually connected with the formation of a vortex ring below the surface [40]. In the case of splashing the liquid surface is greatly disturbed and may lead to the formation of a jet that rises out of the center of the crater formed after impact, above the original surface of the target liquid. This rising liquid column is known as the Worthington jet [43, 44]. Depending on the fluids, a crown with dissipative waves may form at the liquid surface [45]. Right after impact a cavity is formed whose shape is dependent on the impacting liquid drop. The impact energy is important in determining the properties of the phenomena associated with splashing.

This is typically taken into account by considering the Weber number, We, which is a ratio of the kinetic and surface energy [46]. Bouncing and coalescence occur only at low Weber numbers, typically We < 3 [47]. The occurrence of splashing is also dependent on the viscosities of the fluids. Hence, the Reynolds number, a ratio of inertial and viscous forces, is also an important parameter for the splashing limit and the critical Weber number for drop splashing will be a function of the Reynolds number [48]. Entrainment of air bubbles during impact may occur under certain conditions during coalescence and splashing [49, 50].

This thesis investigates the generation of shaped particles produced by the deformation and solidification of molten wax drops in an immiscible cooling medium. Previous research efforts have been primarily directed on the impact of molten metal or paraffin wax drops on a solid surface which generated irregular discs [57-61]. However, there is a gap in the knowledge of the impact and solidification of molten drops in a liquid medium. The interfacial dynamics associated with impinging molten drops on liquid surfaces and the subsequent solidification is complex and not understood in detail. Also, a moving phase interface provides more freedom during the deformation and solidification of the molten drop when compared with a solid surface. In this study, a viscoelastic molten wax material is used for impact at an immiscible aqueous interface to generate non-spherical particles in a controllable fashion.

1.4 Objectives

The main aim of this thesis is to study the fabrication of spherical and non-spherical particles at micro and macro fluid interfaces using droplet microfluidics and molten drop impact at an immiscible liquid interface for application in biomedical diagnostics and consumer goods. To that effect, two materials, polyaniline and wax, were used to generate regular monodispersed particles.

The properties and synthesis of polyaniline, a conducting polymer, has been very well studied and has potential applications in multidisciplinary areas such as electrochromics, chemical sensors, actuators, supercapacitors, rechargeable batteries, toxic metal recovery and bioanlytical sciences like *in vivo* biosensing and continuous monitoring of drugs or metabolites in biological fluids [62-65]. It is versatile, highly conductive, easily doped, inexpensive with favorable redox properties and excellent environmental stability [66]. Although the properties and potentials of polyaniline are well known, to date it has only been synthesized by using self-assembly or template based methods without exact control over their size and morphology [67-70]. Monodispersed micro particles of polyaniline ranging in size from 10 – 100 μm can be used to encapsulate and immobilize biomolecules as they increase the conductivity of the sensor, leading to amplified signals and sensor performance.

Viscoelastic wax based materials are widely used in many applications: dentistry, consumer goods, food processing and drug delivery [71-74]. Their performance and application depends on the particle morphology and size. A new model wax system described previously by Pawar et al. [75] is used in this study to controllably generate non-

spherical particles ranging in the size of mm at interfaces.

The specific objectives are:

1. Fabrication of conduting polymer, polyaniline, microsphers (200 nm - 50 μm in diameter) using droplet microfluidics.
2. Encapsulation of glucose oxidase in polyaniline microspheres for glucose sensing.
3. Manipulation of molten wax drops at an immiscible fluid interface to generate non-spherical particles of diameter in the range of millimeters.

References

[1] A. Imhof and D. J. Pine, Nature 389 (1997), 948.

[2] P. S. Drzaic, Liquid Crystal Dispersions; World Scientific: River Edge, NJ, 1995.

[3] S. Sugiura, M. Nakajima, M. Seki, Langmuir 18 (2002), 3854.

[4] S. Sugiura, M. Nakajima, M. Seki, J. American Oil Chemists' Society 79 (2002), 515.

[5] S.Q. Xu, Z.H. Nie, M. Seo, P. Lewis, E. Kumacheva, H.A. Stone, P. Garstecki, D.B. Weibel, I. Gitlin, G.M. Whitesides, Angew. Chem., Int. Ed. Engl. 44 (2005), 724.

[6] D. Dendukuri, K. Tsoi, T.A. Hatton, P.S. Doyle, Langmuir 21 (2005), 2113.

[7] D. Dendukuri, D.C. Pregibon, J. Collins, T.A. Hatton, P.S. Doyle, Nat. Mater. 5 (5) (2006), 365.

[8] J.P. Rolland, B.W. Maynor, L.E. Euliss, A.E. Exner, G.M. Denison, J.M. DeSimone, J. Am. Chem. Soc. 127 (2005), 10096.

[9] J. Champion, Y. Katare, S. Mitragotri, J. Controlled Release 121 (2007), 3.

[10] G. M. Whitesides, Nature, 442 (2006), 368.

[11] Manz, N. Graber and H. M. Widmer, Sens. Actuators, B, 1 (1990), 244.

[12] A. J. deMello, Nature, 442 (2006), 394.

[13] J. El-Ali, P. K. Sorger and K. F. Jensen, Nature, 442 (2006), 403.

[14] D. B. Weibel and G. M. Whitesides, Curr. Opin. Chem. Biol., 10 (2006), 584.

[15] P. S. Dittrich, K. Tachikawa and A. Manz, Anal. Chem., 78 (2006), 3887.

[16] J. Atencia and D. J. Beebe, Nature, 437 (2005), 648.

[17] H. A. Stone, A. D. Stroock and A. Ajdari, Annu. Rev. Fluid Mech., 36 (2004), 381.

[18] C. Choi, S. Hwang, J. Jeong, S. Kang, J. Kim and C. Lee, Biomed. Eng Lett., 2 (2012), 95.

[19] E. M. Lucchetta, M. S. Munson and R. F. Ismagilov, Lab Chip, 6 (2006), 185.

[20] N. L. Jeon, H. Baskaran, S. K. W. Dertinger, G. M. Whitesides, L. Van de Water and M. Toner, Nat. Biotechnol., 20 (2002), 826.

[21] M. J. Fuerstman, P. Garstecki and G. M. Whitesides, Science, 315 (2007), 828.

[22] L. F. Cheow, L. Yobas and D. L. Kwong, Appl. Phys. Lett., 90 (2007), 054107.

[23] M. Prakash and N. Gershenfeld, Science, 315 (2007), 832.

[24] K. Jensen and A. P. Lee, Lab Chip, 4 (2004), 31N.

[25] G. F. Christopher and S. L. Anna, J. Phys. D: Appl. Phys. 40 (2007) 319.

[26] D. Belder, Angew. Chem., Int. Ed., 44 (2005), 3521.

[27] Kobayashi, K. Uemura and M. Nakajima, Colloids Surf., A, 296 (2007), 285.

[28] R. B. Fair, Microfluidics Nanofluidics, 3 (2007), 245.

[29] D. R. Link, E. Grasland-Mongrain, A. Duri, F. Sarrazin, Z. D. Cheng, G. Cristobal, M. Marquez, D. A. Weitz and Zo, Angew. Chem., Int. Ed., 45 (2006), 2556.

[30] T. Nisisako and T. Torii, Adv. Mater., 19 (2007), 1489.

[31] A. S. Utada, E. Lorenceau, D. R. Link, P. D. Kaplan, H. A. Stone and D. A. Weitz, Science, 308 (2005), 537.

[32] H. Xu, S. W. Li, Y. J. Wang and G. S. Luo, Appl. Phys. Lett., 88 (2006), 3.

[33] E. Chan, B. Lee, P. Ravindra, D. Poncelet, J. Colloid Sci., 338 (2009), 63.

[34] Y. Hu, Q. Wang, J. Wang, J. Zhu, H. Wang, Y. Yang, Biomicrofluidics 6 (2012), 26502.

[35] D.Kannangara and H. Zhang, Colloids Surf A 280 (2006), 203.

[36] R. C. Daniel and J. Berg, Adv. Colloid Interface Sci., 126 (2006), 203.

[37] J. Kim, Int. J. Heat Fluid Flow 28 (2007), 753.

[38] A.N. Lembach, H.B Tan, I.V. Roisman, T. Gambaryan-Roisman, Y. Zhang, C. Tropea, A.L. Yarin, Langmuir 26 (2010), 9516.

[39] A.J Moss and P. Green, Aust. J. Soil Res. 21 (1983), 373.

[40] M. Rein, Fluid Dyn. Res. 12 (1993), 61.

[41] A.L. Yarin, Annu. Rev. Fluid Mech. 38 (2006), 159.

[42] D. A. Bolleddula, A. Berchielli, A. Aliseda, Adv. Colloid Interface Sci., 159 (2010), 144.

[43] P.V. Hobbs and T. Osheroff, Science 158 (1967), 1184.

[44] G.E. Charles and S.G. Mason, J. Colloid Sci., 15 (1960), 105.

[45] B. Peck, L. Sigurdson, Exp. Fluids 18 (1995), 351.

[46] J.M. Cheny, K. Walters, J. Non-Newtonian Fluid Mech. 86 (1999), 185.

[47] L.J. Leng, J. Fluid Mech. 427 (2001), 73.

[48] O.E. Engel, J. Appl. Phys. 38 (1967), 3935.

[49] J. Hallett and L. Christensen, J. Rech. Atmosph. 18 (1984), 225.

[50] R M Schotland, Disc. Faraday Soc. 30 (1960), 72.

[51] J. J. Thompson and H. F. Newall, Proc. R. Soc. London 39 (1885), 417.

[52] A. Prosperetti, H.N. Oguz, Philos. Trans. R. Soc. London Ser. A Math. Phys. Eng. Sci. 355 (1997), 491.

[53] H.N. Oguz, A. Prosperetti, A.R. Kolaini, J. Fluid Mech. 294 (1995), 181.

[54] S.T. Thoroddsen, T.G. Etoh, K. Takehara, J. Fluid Mech. 478 (2003), 125.

[55] C. Clanet, C. Beguin, D. Richard, D. Quere, J Fluid Mech. 517 (2004), 199.

[56] H. Aryafar and H.P. Kavehpour, Phys. Fluids 18 (2006).

[57] R. Bhola, S. Chandra, J. Materials Science, 34 (1999), 4883.

[58] G. Trapaga, E.F. Matthys, J.J. Valencia, and J. Szekely, Metallurgical Transactions 23B (1992), 701.

[59] S. Inada and W. J. Yang, Experimental Heat Transfer, 7 (1994), 93.

[60] S. Schiaffino and A.A. Sonin, Physics of Fluids, 9 (1997), 3172.

[61] S. D. Aziz and S. Chandra, International Journal of Heat and Mass Transfer, 43 (2000), 2841.

[62] S.B. Adeloju and G.G. Wallace, Analyst, 121 (1996), 699.

[63] G.W.J. Harwood and C.W. Pouton, Adv. Drug. Deliv. Rev., 18 (1996), 163.

[64] T. Ahuja, I.A. Mir, D. Kumar and Rajesh, Biomaterials, 28 (2007), 791.

[65] S. Palaniappan, A.C. Ford, D. Greer, S.M. Everett, D.M. Chalmers, A.T.R. Axon and P.J. Hamlin, Inflamm Bowel Dis I., 13 (2007), 1488.

[66] Y.D. Liu, B.J. Park, Y.H. Kim and H.J. Choi, J. Mater. Chem., 21 (2011), 17396.

[67] I. Sapurina and J. Stejskal, Polym Int, 57 (2008), 1295.

[68] L. Zhang and M. Wan, Adv. Funct. Mater., 13 (2003), 815.

[69] L. Zhang, M. Wan and Y. Wei, Synth. Met., 151 (2005), 1.

[70] Y. H. Huo, H. Zhang, J. Jiang and Y. Yang, J. Mater, J. Mater. Sci., 47 (2012), 7026.

[71] R. G. Craig, (1985) Restorative dental materials 7th ed. St. Louis: Mosby

[72] E. Endlein and K.H Peleikis, SOFW Journal 2011.

[73] R. Kamble, M. Maheshwari, A. Paradkar, S. Kadam, AAPS PharmSciTech, 5 (2004), 75.

[74] R. Sridhar and S. Ramakrishna, Biomatter 3 (2013).

[75] A. B. Pawar, M. Caggioni, R. W. Hartel, P. T. Spicer, Faraday Disc. 158 (2012), 341.

Chapter 2

Fabrication and Characterization of Polyaniline Microspheres using Droplet Microfluidics

2.1 Introduction

The Nobel Prize in Chemistry in the year 2000 recognized the discovery and development of conductive polymers (CP) and their varied electronic properties. CP have potential applications in multidisciplinary areas such as electrochromics, chemical sensors, actuators, supercapacitors, rechargeable batteries, toxic metal recovery and bioanlytical sciences like *in vivo* biosensing and continuous monitoring of drugs or metabolites in biological fluids [1-5]. CP can be used to encapsulate and immobilize biomolecules as they increase the conductivity of the sensor, leading to amplified signals and sensor performance. Due to unusual effects associated with particular surfaces, quantum sizes, macroscopic tunneling, CP nanostructures have exhibited superior properties to those of their bulk counterparts [6-8].

One of the most well studied CP is polyaniline (PANI). PANI is of considerable interest as it is versatile, highly conductive, easily doped, inexpensive with favorable redox properties and excellent environmental stability [9]. Although the properties and potentials of PANI are well known, to date PANI has only been synthesized by using self-assembly or template formations without exact control over their size and morphology [10-12]. Variations in the chemical oxidation of aniline have produced ‘‘polyaniline’’ possessing a wide variety of micro-

and nanoscale structures – nanofibers, nanotubes, microsphere, granules [13-15]. Various nanostructures of PANI have been synthesized – nanofibers, nanowires, nanofilms, microspheres, nanodiscs, nanoplates, hollow shells [16-18]. However, monodispersed microspheres are of particular importance, especially for biomedical applications, because of their increased surface area and lower contact resistance as compared to nanotubes or other nanostructures for sensing or encapsulation, reliable individual performance and increased efficiency [19-25]. Uniform polymer microspheres have found extensive applications in various fields such as clinical diagnosis, spacers in large liquid crystal displays, fillers in advanced composites, chromatography, and waste water treatment [27, 28].

Microfluidics has made significant advances in the past decade in the area of producing monodisperse emulsion droplets. Synthesis of monodispersed microspheres using microfluidics has many advantages over bulk emulsion processes, including lower emulsion polydispersity indices and accessibility to a wider range of microsphere shape [29]. Droplet microfluidics usually involves water-in-oil emulsions to compartmentalize reagent into picoliter volumes for rapid transport, mixing and reaction [30-34]. These micron size droplets can be functionalized with nanoparticles or molecules inside the droplet phase or on the surface for applications such as immunoassays and high throughput screenings. The microfluidic techniques to form micron and nano sized particles with controlled shape and morphology could eliminate the need to rely on PANI self-assembly or template formations and further increase the range of applicability of this CP.

The significance of this study lies in the major effort to use microfluidics creatively to synthesize PANI microspheres for biosensing and controlled release. The knowledge gained

from this project will provide: (1) a new versatile method to achieve fabrication of microspheres for sensing and controlled release; (2) enhanced fundamental understanding of the relationships between microfluidic processing, materials properties and performance for biomedical applications and (3) the development of the synthesis route for glucose detection can open up new pathways for bioencapsulation and controlled release. The study can be extended to continuous glucose sensing by designing enzyme sensors for implantation into the dermis or subcutaneous regions of the skin and measure the current or voltage change associated with the enzyme activity on detection of the recognition elements. Biocompatible PANI nano-micro-spheres that undergo conformation changes depending on their environment may also be used as "smart materials" for controlled in vivo drug release.

In this study, a new synthesis route for the fabrication of PANI composite microspheres using microfluidics is developed. The specific aims are listed below.

1. Develop a microfluidic device to create monodisperse PANI microspheres (200 nm - 50 μm in diameter) in oil.

2. Perform detailed surface characterization using SEM, EDX, UV/Vis spectroscopy and conductivity studies on PANI dry spheres by varying the molar ratio at fixed room temperature.

2.2 Materials and Methods

2.2.1 Materials

Slygard 184 silicone elastomers kits (polydimethylsiloxane, PDMS, and curing agent) were purchased from Dow Corning Co (Midland, MI). SU-8 2035 photoresist, 4 inch silicon wafers, peroxide-cured silicon tubing (ID 0.76 mm, Cole Palmer), BD plastic syringes of 1 ml volume, 26 gauge Sub-Q luer lock needles, 0.38 mm ID polyethylene tubing and multiple syringe pumps from Harvard Apparatus were used. Ammonium persulfate (APS), Aniline (Ani), 1-4 phenylenediame (p-PDA), Span 85 and hydrochloric acid (HCl) were used as received from Sigma-Aldrich without further purification. Deionized water and hexadecane were used as the phase solvents.

2.2.2 Fabrication of Microfluidic Devices

A T-junction device is used to generate polymer micropsheres. Channel designs were created using a drawing software, Layout Editor. Silicon wafers were prepared by sequentially washing with acetone, isopropyl alcohol and DI water. Then, the wafer was spin-coated with SU-8 2050, a negative photoresist (MicroChem Corp. MA), at the thickness desired for the final channel height (30-100 um). The wafer was pre-baked on a programmable hot-plate following a procedure that depends on the SU-8 type and thickness. The channel pattern is exposed on the SU-8 coated silicon wafer using a Heidelberg μPG 101 laser pattern generator (Heidelberg Instruments GmbH, Heidelberg, Germany). After exposure, the wafer was hard baked following a procedure similar to the pre-bake. The design was then developed using a standard SU-8 developer. Development time is dependent on the SU-8 thickness. The spin-coat programs,

baking procedures and development times were provided by manufacturers. Development was stopped by rinsing the wafer with IPA followed by DI water. The final step for wafer preparation is surface modification. The wafer was placed in a desiccator containing a dish with a few drops of tridecafluoro-1,1,2,2 tetrahydrooctyl trichlorosilane that was evaporated onto the wafer surface and served as a release layer to ensure release of the PDMS. The microfluidic devices were then fabricated using standard soft-lithography techniques [35]. The microfluidic platform consisted of a PDMS fluid layer fabricated using 10:1 ratio of the pre-polymer and crosslinker. The inlet and outlet ports made of silicone (peroxide-cured) of 0.76 mm inner and 2.79 mm outer diameter (Cole-Parmer Instrument Company, Vernon Hills, IL) were fastened to the wafer using model glue (Testor Corp, Rockford, IL) before the PDMS layer is poured. It is then placed in a vacuum pump to remove air bubbles and cured at 65 ^{o}C overnight in an oven. The patterned PDMS substrate was bonded irreversibly to a glass slide after plasma treatment in a plasma chamber (PDC32G, Harrick Plasma, NY, USA) at 10.5 W power at 300 mTorr for 60 seconds. If necessary, the bonded side of the PDMS can be pre-cleaned with transparent tape. This step is often necessary if the devices are not made in a clean room or if the time between peeling and bonding is long. The molded layers and base layers are placed into the chamber with the side to be bonded facing up. Immediately after treatment, the layers are removed from the chamber and firmly pressed together. Test fluids are contained in any of a variety of luer lock type syringes capped with 26 gauge Sub-Q needles. The ports are connected to the syringe needles by 0.38 mm ID polyethylene tubing. Flow from each syringe is controlled by a pressure controlled syringe pump from Harvard Apparatus.

2.2.3 Polymerization of Aniline

PANI is synthesized from the chemical oxidative polymerization of aniline monomer using the free radical initiator and chemical oxidant, ammonium persulfate (APS). PANI has three oxidized forms – pernigraniline, leuco-emeraldine, and emeraldine base. Polyaniline being redox active can be switched between various oxidized and reduced forms by varying the acidity of the polymerization medium. Amongst the three oxidized forms, the emeraldine base is the most stable and exhibits higher conductivity when protonated, characterized by an absorption peak at approximately 320 nm [30]. Aniline monomer can be oxidized by APS to form PANI (emeraldine) in an acidic medium, with sulfuric acid as one of the byproducts. The polymerization of aniline is a two-step process in which the pernigraniline salt is first formed and then reduced to the emeraldine salt when aniline monomer gets oxidized to the radical cation. In our work, we aimed to generate stable and conducting PANI microspheres in the emeraldine form and the polymerization is carried out in the presence of 0.5 M hydrochloric acid to enhance the production of the emeraldine salt form. The time for polymerization estimated from the bulk mixing of 1 μL of APS droplet in an excess of aniline in oil and scaled to a 50 μm sized PANI microsphere is approximately 15 seconds. For bioencapsulation and biosensing applications, the emeraldine state of PANI is highly desired as it increases the conductivity of the microsphere, which can amplify the detection signal. For the microsphere production, the oxidant ammonium persulfate (APS) was used to carry out oxidative chemical polymerization (Figure 2.1).

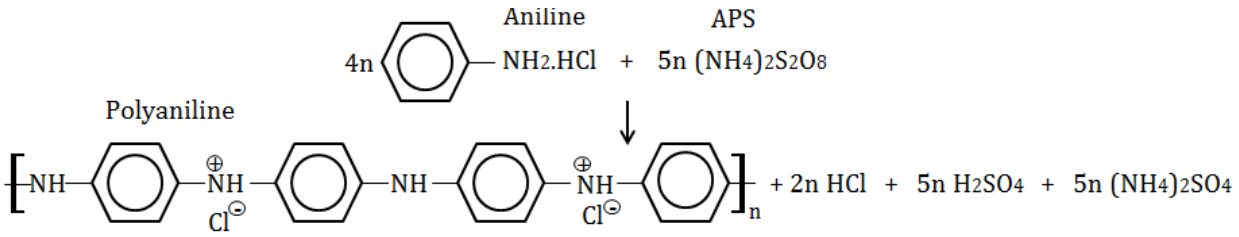

Figure 2.1. Aniline monomer in the presence of hydrochloric acid gets oxidized by ammonium peroxydisulfate to form polyaniline (emeraldine) in an acidic medium with sulfuric acid as one of the byproducts.

2.2.4 Characterization of the Microspheres

Morphologies of the PANI microspheres were obtained by using a field emission scanning electron microscope (SEM, FEI Sirion) with an acceleration voltage of 5 kV. 2 μL of the PANI microspheres aqueous dispersion was deposited on a carbon/formvar TEM grid (Ted Pella Inc, CA) and air dried at room temperature. The chemical compositions of the microspheres was detected by using SEM combined with Energy Dispersed X-ray Spectrometer system (SEM-EDX, FEI Sirion) at an accelerated voltage of 20 kV, and UV-Vis spectroscopy. The absorbance of PANI microspheres was measured and the wavelength at which the peak of the absorbance curve occurred was recorded on a UV/Vis spectrometer (Varian Cary 5000 UV/Vis/NIR). A two-point probe technique was used to calculate the electrical conductivity of the PANI microspheres using a voltage-current picoammeter. All shown results were from one day-old samples unless specified otherwise.

2.2.5 Modeling

Finite element analysis was conducted by COMSOL Multiphysics to study the electrical conductivity of a single PANI sphere. The modeling results combined with the experimental

observations will allow relatively accurate measurement of the conductivity as compared to only experimental measurement as there is limited information of the current distribution within the microsphere. A solid sphere between a probe and a planar electrode was modeled as 2D axisymmetric. The resulting current density distribution due to an applied potential of 0.4 V was computed and the total current through the particle was calculated by integrating the current density across the cross section. Pouillet's law (Eq 2.1) was used to calculate the conductivity (σ) using the current (I) calculated above at a fixed potential (V = 0.4 V), the diameter of the microsphere (l) and the cross-sectional area of the current density (A).

$$\sigma = {I}\Big/{\frac{Vl}{A}} \tag{2.1}$$

Using COMSOL simulation, based on the best curve fit, the conductivity was obtained as a function of the current I as:

$$\sigma = \frac{I}{272} \tag{2.2}$$

(see more details in Results). The conductivity of the PANI microsphere was then calculated using I obtained experimentally from the 2-point probe measurement of the $I - V$ curve at 0.4 V.

2.3 Results

2.3.1 Polyaniline Microsphere Production

A T-junction device was employed with three inlets and one outlet. An oil phase containing hexadecane and a surfactant, SPAN 85, was pumped through the first inlet and an aqueous dispersed phase containing APS through the second inlet (Figure 2.2). The APS droplet formed at the first T-junction would be polymerized by the aniline (in an oil phase) introduced at the third inlet. The polymerized aniline microspheres (PANI) were then transported out of the microfluidic chip through the outlet.

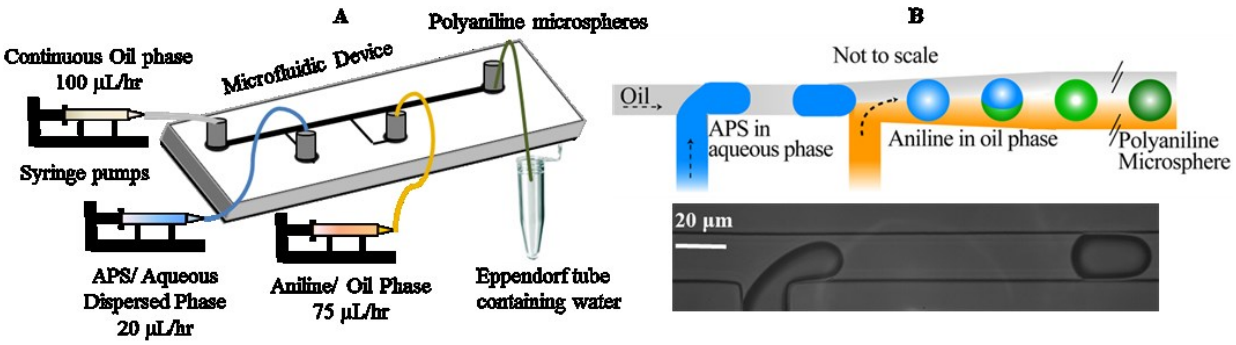

Figure 2.2. Polyaniline droplets were produced in a T-junction microfluidic device containing a two continuous phases, aniline and hexadecane, and one dispersed phase, APS. The polymerized aniline droplets were transported off-chip through an exit.

Proper solvents and channel dimensions were chosen to promote the interfacial diffusion of aniline into the dispersed phase so that the polymerization could be completed on-chip. The continuous oil phase was hexadecane containing Span 85 (20% w/w) to prohibit coalescence of droplets in the microchannel (1st inlet). The dispersed phase consisted of 0.2 M or 0.4 M APS

with 0.5 M HCl in deionized water (2nd inlet). The second continuous phase was Span 85 (20% w/w), 0.2 M Aniline and 5 mM p-phenylenediamine (pPDA) in hexadecane (3rd inlet). The use of 5 mM pPDA and HCl enhances the polymerization rate between APS and Aniline [31]. Droplets were formed with a continuous phase flowing at 100 µl/hr and a dispersed phase at 20 µl/hr. The measured interfacial tension between the oil phase and aqueous phase was σ = 30.4 mN/s and their viscosities were $\eta 1$= 5.83 mPa.s and $\eta 2$ =1.00 mPa.s. A shear rate of 11.0 s^{-1} at the T-junction generated by the oil phase in the microchannel led to APS droplet breakup as a result of the competition between capillary force and viscous force. The capillary number (Ca= $\eta 1 U/\sigma$) for the APS droplet production is 9.52 x 10^{-3} and falls within the range for droplet breakup for the above channel dimensions. Shortly after the APS droplet production, a concentrated aniline solution (3rd inlet, mixed with 20% wt/wt Span 85, 0.2 M Aniline and 5 mM pPDA in hexadecane) was introduced at 75 µl/hr to mix with the inert hexadecane continuous phase and prompted interfacial diffusion (Figure 2.2). This step prevented accumulation of polymerized aniline at the semi-motionless interface created at the first T-junction. Nanostructured PANI formed instantaneously while the aniline was polymerized at the APS droplet interface. The hydrophilic PANI diffused from the APS droplet interface into the aqueous core and acted as nucleation sites throughout the APS droplet and eventually led to polymerized PANI microspheres (Figure 2.3) [32] The polymerized PANI microspheres were transported off the chip and collected in a water bath to remove the oil phase. The microspheres were washed again with DI water and dried at room temperature for further characterization.

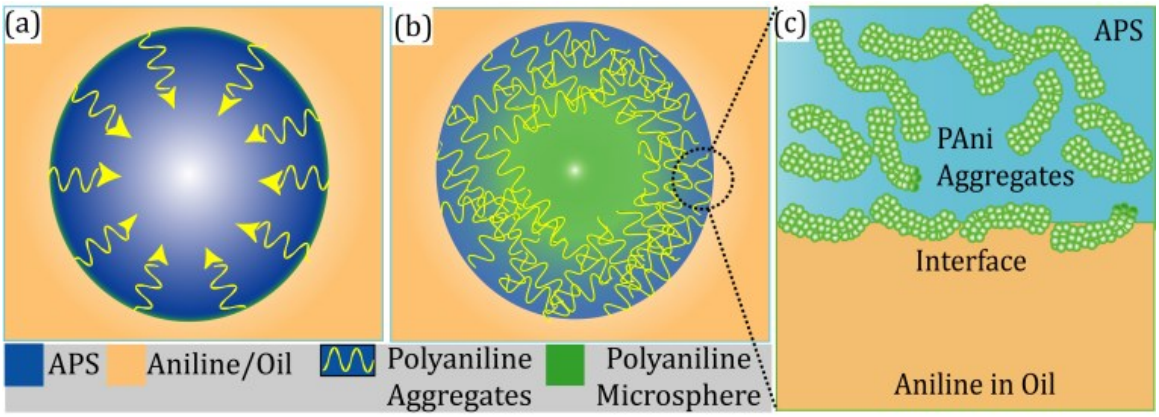

Figure 2.3. (a) Aniline (in orange) interacts with APS (in blue) droplet at the interface and forms polyaniline nanostructures (in yellow). Polyaniline being hydrophilic diffuses into the APS droplet and starts aggregating inside the droplet (b) Polyaniline aggregates form interlinked layers leading to a microsphere (c) Polyaniline nanostructures formed at the interface of the aqueous and oil phase diffuse into the aqueous phase.

2.3.2 Morphology of the Polyaniline Microspheres

The dried microspheres were stored at room temperature (25°C) and exposed to air. Their surface morphology and elemental composition were monitored over a month by using SEM and EDX. All the images are captured from one day-old samples. The PANI microspheres were fairly monodispersed with a deviation of less than 2% (Figure 2.4 (c)).

Emeraldine salt form of PANI is green in color and its base form is blue. After complete polymerization, all the PANI microspheres were green in color, indicating their emeraldine salt form. They were approximately 50 µm in diameter with a porous polymerized PANI outer layer, which consists of fibril structures of diameters 200 – 500 nm, as shown in Figure 2.4 (b). The layer contains pores between 300 nm - 1µm and fibrils of diameter ~150 nm, distributed at

random orientations. The morphology of the fibrils observed in the SEM images is dependent on the amount of HCI doping and the amount of initiator, p-PDA. The rate of polymerization was enhanced by the addition of initiator p-PDA as it accelerated the polymerization rate which favored homogenous nucleation over heterogeneous nucleation. The initiator molecules could serve as the nucleation center for the polymer chain growth, leading to the formation of fibrils [33, 34].

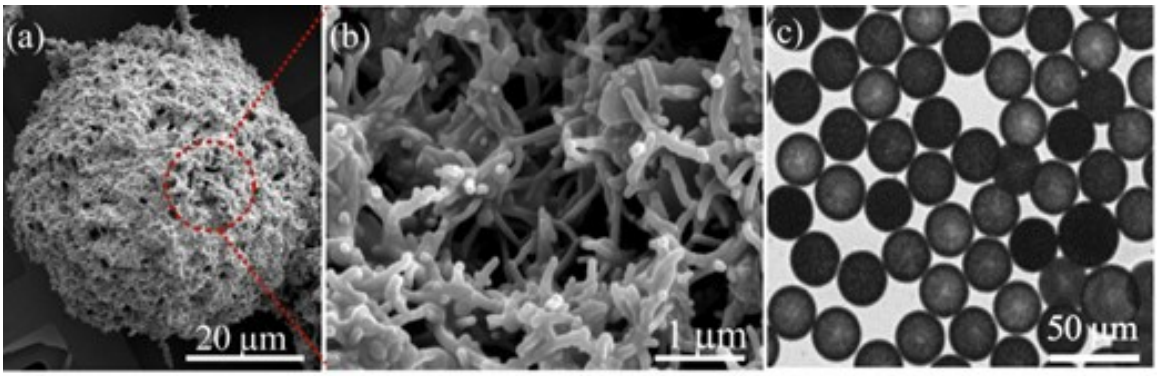

Figure 2.4. SEM images of a 0.4 M (APS/Aniline = 1:1) PANI microsphere 2 hours after fabrication in the present study are shown above. (a) The PANI microsphere has a porous structure with a polymerized aniline outer layer. (b) A magnified image of the microsphere shows the porous morphology. (c) An optical microscopy image shows monodispersed microspheres transported off chip at different stages of polymerization as indicated by their color.

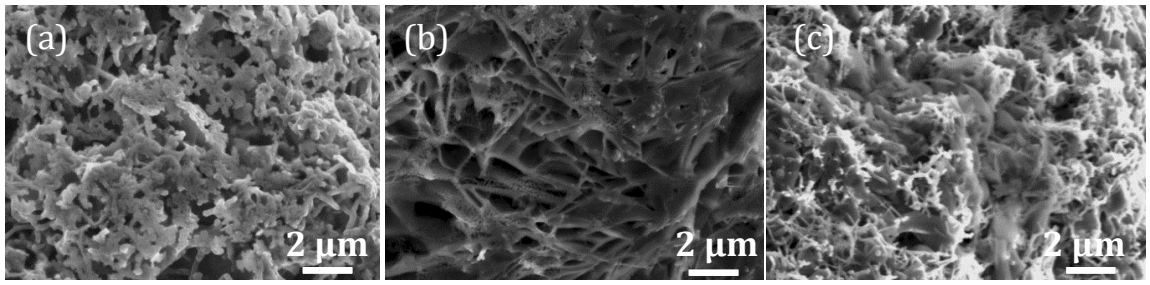

Figure 2.5. SEM images of the surface morphology of the three different molar ratios are shown in (a) 0.2 M (2:1) (b) 0.2 M (1:1) (c) 0.4 M (1:1).

The extent of polymerization varied with the molar ratio and the concentration of APS and aniline (Figure 2.5). From the SEM images, it was observed that the 0.2 M PANI spheres of 2:1 ([APS]/[Aniline]) molar ratio had a more homogeneous and less porous layer as compared to the 1:1 molar ratio spheres (Figure 2.5a). The 0.2 M (1:1) PANI spheres had a more porous outer layer as compared to the 0.2 M (2:1) and 0.4 M (1:1) PANI spheres (Figure 2.5b). In the 0.4 M (1:1) microspheres, the higher concentration of APS and aniline led to faster polymerization which caused inhomogeneous aggregation of the nanostructures (Figure 2.5c). The morphologies can be varied by changing the molar ratio of [APS]/[Aniline] and the level of doping and additives. The PANI spheres were solid and had uniform oxidation from the edge to the center (Figure 2.6a).

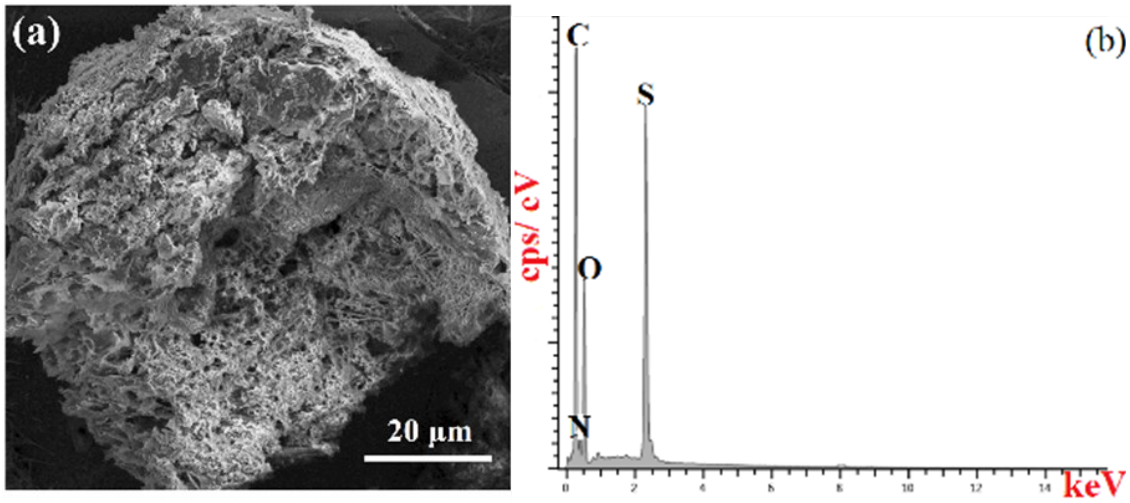

Figure 2.6. (a) SEM image of the cross section of a 0.4 M (APS/ Aniline = 1:1) PANI microsphere 1 day after fabrication is shown. It is uniformly dense from edge to center. (b) EDX analysis across the cross section of the microsphere does not show a significant variation from the chemical composition on the surface. It has trace amounts of chlorine and copper present from the byproducts and the copper tape on which the grid containing the sphere is placed.

The chemical composition of the microspheres was measured by EDX (Figure 2.7, Figure 2.8, Table 1). EDX Analysis showed a higher percentage of carbon in 0.2 M (2:1) spheres as compared to 0.2 M (1:1) and 0.4 M (1:1) spheres (Table 1) which could imply a different orientation of the polymer chains in the 2:1 molar ratio spheres. EDX analysis across the cross section showed no significant variation in the internal chemical composition as compared to the surface (Figure 2.6b). The presence of oxygen may be due to the bound water molecules or/and, from partial oxidation of the PANI chains. The presence of sulfur is partly due to the residual sulfate counter ions produced by the reduction of APS during polymerization [36]. All PANI microspheres showed no significant difference in the elemental composition of the surface or morphology over a 1 month period. This important result is encouraging for potential

encapsulation and drug delivery applications as the instability of the storage medium affects the performance of the device.

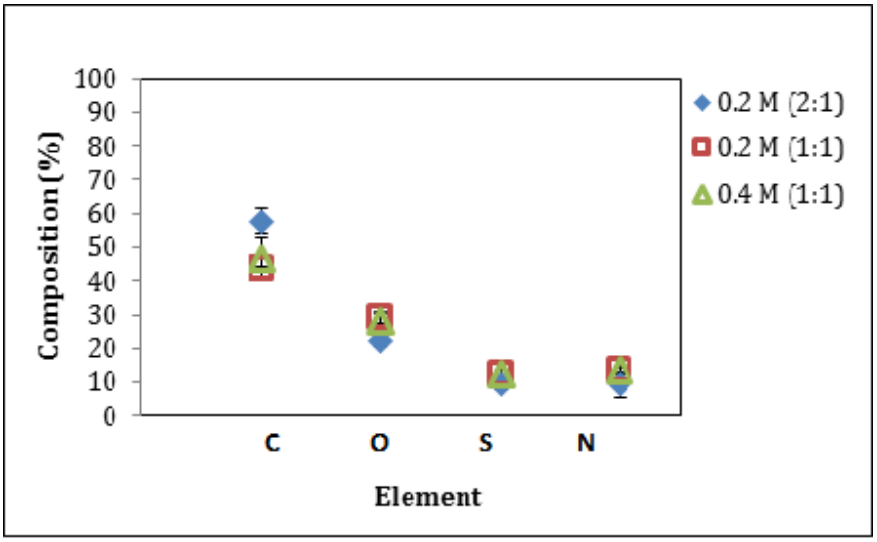

Figure 2.7. A comparison of the surface elemental composition of the polyaniline spheres measured using Energy Dispersed X-ray Spectrometer one day after fabrication is shown.

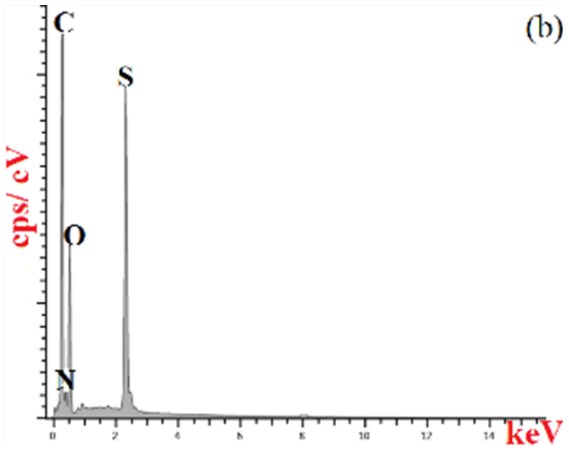

Figure 2.8. The EDX spectrum of a 0.2 M (1:1) microsphere is shown.

Table 2.1. Elemental Composition of the surface of the polyaniline spheres measured using Energy Dispersed X-ray Spectrometer one day after fabrication.

Molar Ratio	C (%)	O (%)	S (%)	N (%)
0.2 M (2:1)	57.77 ± 3.95	22.03 ± 1.76	9.23 ± 1.27	9.27 ± 3.72
0.2 M (1:1)	43.47 ± 0.76	28.87 ± 1.65	12.30 ± 1.04	13.20 ± 0.92
0.4 M (1:1)	46.47 ± 6.45	27.93 ± 2.97	12.37 ± 1.17	13.73 ± 0.85

2.3.3 Optical Spectroscopy

For conducting polymers, optical spectroscopy is an important technique to understand the conducting states corresponding to the absorption bands of inter and intra-gap states [37]. A 5 μL suspension of PANI microspheres in water was evaporated and stored for a day at room temperature to form a uniform multilayer film of dry microspheres on a glass slide. The UV-Vis spectrum of the film of microspheres on the glass slide was recorded. The UV-Vis spectra of the one day-old PANI microspheres showed three characteristic absorption bands at ~322 nm, ~435 nm, and ~813 nm, which is characteristic of PANI in the emeraldine salt form [38-40] (Figure 2.9a). The peak of wavelength 306–324 nm for PANI in the emeraldine salt is due to the π–π* transition of benzenoid ring; the peak of wavelength band 402–420 nm is due to the polaron–π* transition, and the peak in wavelength band 800–835 nm is attributed to the π–polaron transition. In addition, the peaks in wavelength bands of 402–420 nm and 800–835 nm arise owing to the doping level and the formation of polarons [38]. The absorbance spectrum occuring in 0.2 M (2:1), 0.2 M (1:1) and 0.4 M (1:1) microspheres is shown in Figure 2.9a and a comparison of the absorbance peaks is shown in Figure 2.9b**,** showing no significant variation. The absorbance of

the microspheres stored at room temperature was measured over a month. There was no significant shift in the peaks, indicating that the PANI microspheres remained in the emeraldine state for one month.

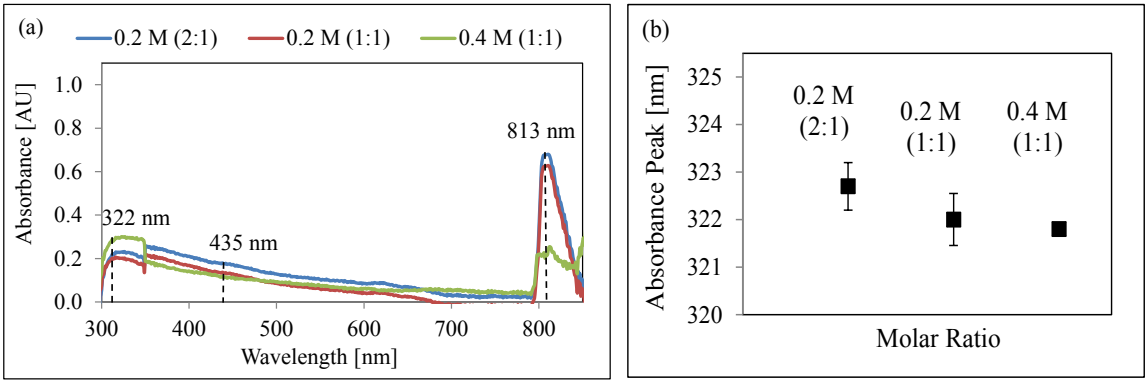

Figure 2.9. (a) Absorption spectrum of the three different type of PANI microspheres show peaks characteristic to that of emeraldine in the salt form. Peaks occurred at ~322, ~435 and ~813 nm. (b) The average of five replications of PANI microspheres is reported for the position of absorbance peaks in 1:1 (APS: Aniline) molar ratio and 2:1 molar ratio.

2.3.4 Conductivity of the Polyaniline Microspheres

PANI is a conducting polymer whose conductivity depends on the oxidation state. The conductivity of PANI has been conventionally studied by measuring the *I-V* curves of compressed pellets of the micro- or nano structures using a standard two or four-probe method [41]. A 5 µL suspension of PANI microspheres in water (one day old) was deposited on a gold electrode and dried at room temperature. A two-point probe technique using a tungsten probe was employed to measure the *I–V* curves of the individual microspheres from 0 ~ 1 V at room temperature and the resistance was calculated from the slope of the *I-V* curve (Figure 2.10). To

analyze the conductivity of a PANI microsphere, a 2D axisymmetric model using CCOMSOL Multiphysics program was constructed (Figure 2.11).

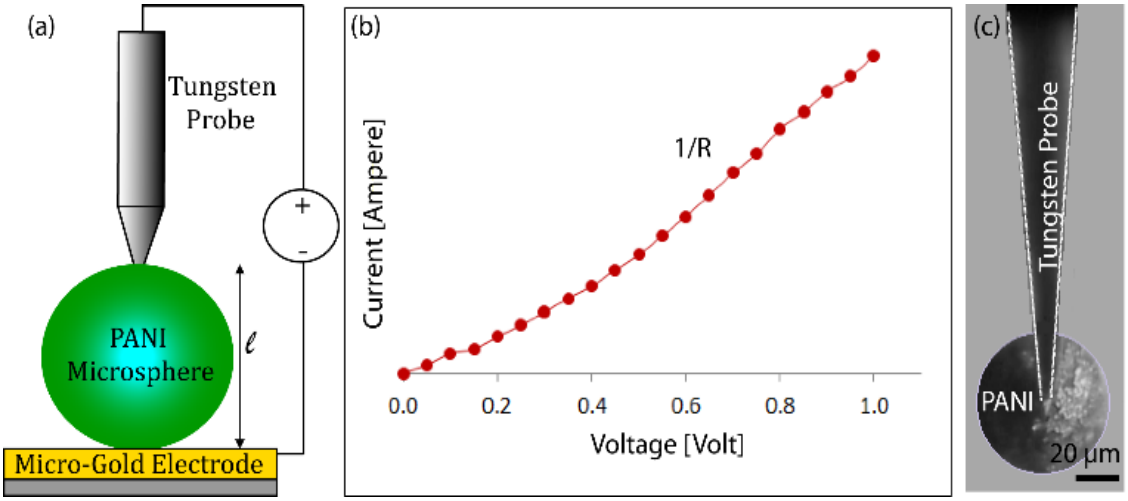

Figure 2.10. PANI microspheres were deposited on a gold electrode and their resistance was measured using a two-point probe method. (a) A schematic of a PANI microsphere deposited on a micro-gold electrode is shown. A two-point probe method was used to measure the bulk resistance of the microsphere. (b) A voltage sweep from 0 – 1 V was applied to the microsphere and the resistance was calculated from the slope of the *I-V* curve. (c) An optical image of the PANI microsphere and the tungsten probe is shown.

The current measured from the two-point probe technique at 0.4 V was then compared with the simulated current and the corresponding conductivity values were computed. In the experiment to measure conductivity of the PANI microsphere, cross-sectional diameter was used to apply a constant voltage potential of 0.4 V between the tip and bottom of the sphere. The surrounding medium was assumed to be insulated. Since the tip and the gold surface had very low resistance, the measured resistance was due to the PANI microsphere. In our measurement using three different diameters of spheres, the contact resistance between the probe and

microsphere was negligible in comparison to the resistance of the PANI microsphere which was in the range of mega ohms (Figure 2.12). Thus the current from the numerical model could be directly compared with the measured current of the PANI sphere.

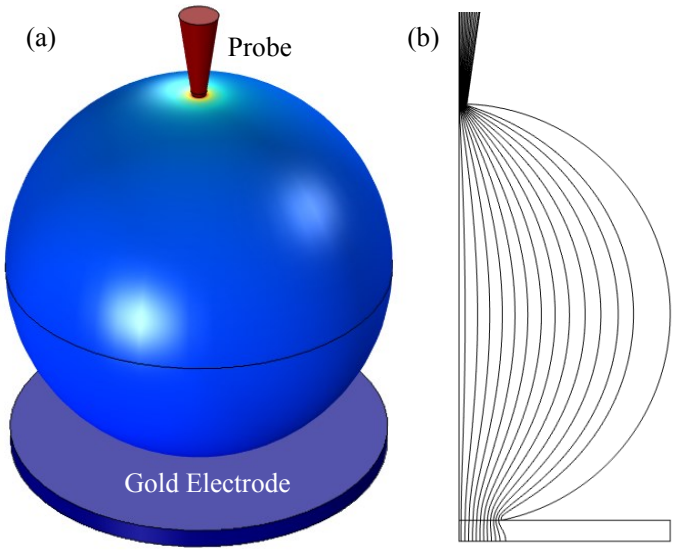

Figure 2.11. (a) 2D axisymmetric model of a solid sphere (diameter: 50 µm) between a probe and a planar gold electrode. (b) Current density distribution in the sphere between the probe and the gold electrode.

The probe tip of 4 µm diameter was assumed to penetrate 1 µm inside the sphere in the radial direction. The resulting current density distribution in the sphere due to an applied potential of 0.4 V between the probe and the gold electrode was solved by setting the potential of 0.4 V at the top of probe and the ground condition (V = 0) at the bottom of the sphere. The total current through the sphere was calculated by integrating the current density over the cross sectional area of the sphere center using trapezoidal numerical integration (Equation 1, Figure 2.13).

$$I = \int_0^R f(r) r dr \int_0^{2\pi} d\theta \tag{2.3}$$

where *f(r)* is the current density extracted from the model above. Pouillet's law (Equation 2.1) was used to compute the conductivity from the current.

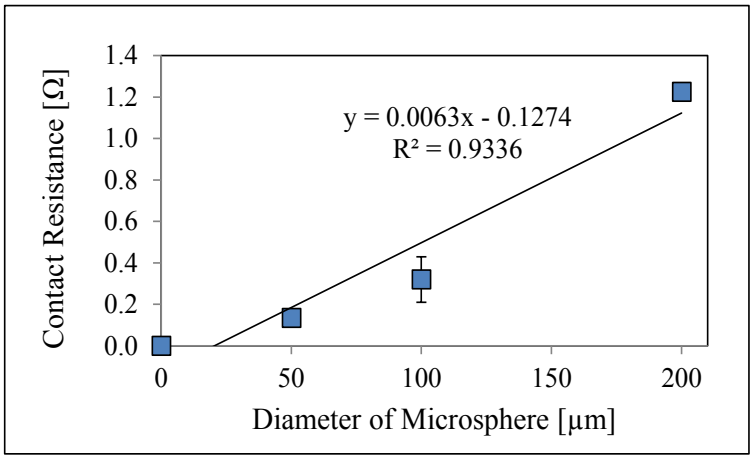

Figure 2.12. The contact resistance for PANI microspheres of diameters ~50 µm, ~100 µm and ~200 µm was found to vary linearly with the diameter of the microsphere. The contact resistance was negligible as compared to the bulk resistance of the microsphere which was in the mega ohm range.

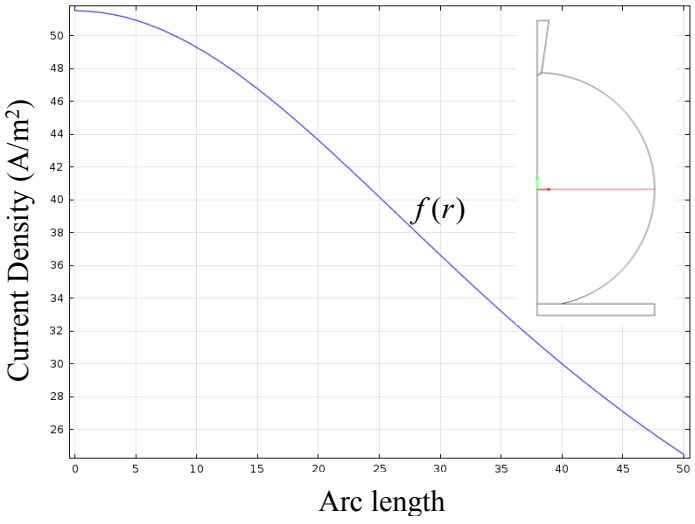

Figure 2.13. Current density over the cross sectional area at the sphere center (the red line in the inset figure) was calculated.

The result shows the linear relation between the current through the sphere and the conductivity of sphere with the applied potential of 0.4 V (Figure 2.14). The variation of the current with the penetration depth of the probe into the microsphere was also computed with the conductivity of 0.001 S cm^{-1} (Figure 2.15). The current change between 1 µm and 5 µm was less than 0.2 µA, which could be neglected for the estimation of the conductivity.

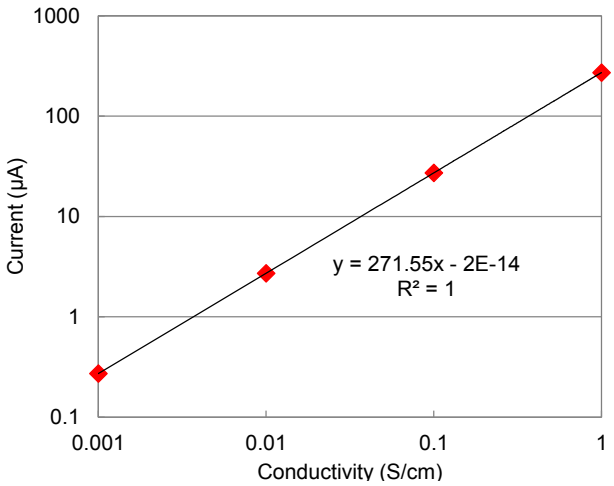

Figure 2.14. There is a linear variation between the current and the conductivity values of a solid sphere.

Using the linear relation between current and conductivity obtained from the model, the conductivity values of the PANI microspheres were calculated from the experimental current values measured at 0.4 V using the two-point probe method. The specific electrical conductivity of the 0.2 M 2:1 ([APS]/[Aniline]) molar ratio microspheres were measured to be in the range of 10^{-3} S cm^{-1} . However, the values for the 0.2 M and 0.4 M of the 1:1 molar ratio microsphres were lower by two orders of magnitude (Table 2.2). Due to the lower amount of APS present in the 1:1 molar ratio microspheres, the excess aniline could have reduced the polyaniline formation

and led to lower conductivity values as compared to the 2:1 molar ratio microspheres. Contact resistance between the probe and the microspheres was measured to be negligible and the conductivity was mainly derived from the bulk of the microsphere. The conductivities reported by Long et al. in 2004 for β-naphthalene sulfonic acid and salicylic doped hollow polyaniline microspheres of diameters 0.2 – 7 μm using 1:1 ([APS]/[Aniline]) molar ratio were in the range of 10^{-4} – 10^{-2} S cm^{-1}. The conductivity for the 0.2 M 2:1 molar ratio PANI microspheres in our work is in the same range as those reported by other groups using either self-assembly or template methods [42, 43].

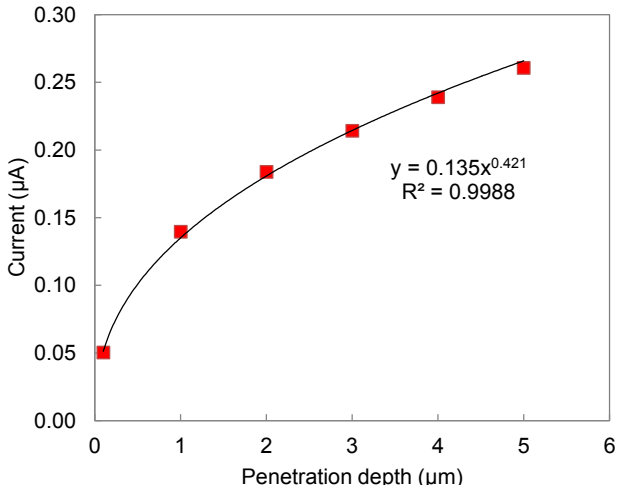

Figure 2.15. The variation of current with the penetration depth of the probe inside the microsphere is shown.

Table 2.2. The specific conductivity of the PANI microspheres with different molar ratios and APS concentrations and a probe penetration depth of 1 μm.

Molar Ratio	Average Specific Conductivity [S cm^{-1}]
0.2 M (2:1)	57.77 ± 3.95
0.2 M (1:1)	43.47 ± 0.76
0.4 M (1:1)	46.47 ± 6.45

However, the size of the microspheres in this work is much larger and the conductivity is expected to increase by decreasing the size of the sphere due to an increase in the interchain conductivity [44, 45].

The ongoing effort is to enhance the conductivity of PANI microspheres by scaling down the particle size to sub-microns. Satellite droplets in sub-micron size can be generated using droplet microfluidics and hydrodynamic instability [46]. During drop formation within a flow focusing microfluidic channel, the droplet can break off into a primary droplet and a satellite droplet due to hydrodynamic instability, which can be obtained by lowering the flow rate of the dispersed phase. The satellite droplets can be separated from the primary droplets by exploiting the difference in their densities or sizes [47]. Nevertheless, our work demonstrates that the microfluidic synthesis approach provides a simpler, faster, and higher throughput method for PANI production as compared to the self-assembly or template methods.

To investigate the stability of the dry PANI microspheres, they were stored them at room temperature (25°C) under vacuum. The specific conductivity of PANI microspheres was measured over the period of one month. The conductivity values of the 0.2 M (1:1) and the 0.4

M (1:1) microspheres decreased exponentially by 84% and 62% respectively. However, there was no obvious change in the specific conductivity of the 0.2 M (2:1) microspheres. The decrease in conductivity of the 1:1 molar ratio microspheres could be due to the loss of moisture caused by the large surface area or decreasing levels of protonation caused by a decrease in charge carriers [48, 49]. The 0.2 M (2:1) microspheres were resistant to loss in moisture comparatively, showing a greater stability and will be used for future experiments.

2.3 Conclusion

In this study, droplet microfluidics approach was used to provide an easy, one-step procedure to synthesize monodispersed PANI microspheres. The morphology of the polymerized PANI microspheres is fibrillar and porous in nature which can be controlled by varying the initial reaction conditions. The conductivity of the individual PANI microspheres was in the range of 10^{-5}-10^{-3} S cm^{-1}. Hollow PANI microspheres can also be generated using our microfluidic technique by synthesizing aniline droplets as the dispersed phase and treating it with APS in the continuous aqueous phase. The porous PANI microspheres possess great potentials in the fields of biosensing, solar conducting cells, and drug delivery due to their conducting nature and biocompatibility. Our next step is to explore the use of the PANI microspheres for encapsulation of glucose oxidase enzyme for glucose sensing.

References

[1] S.B. Adeloju and G.G. Wallace, Analyst, 121 (1996), 699.

[2] G.W.J. Harwood and C.W. Pouton, Adv. Drug. Deliv. Rev., 18 (1996), 163.

[3] T. Ahuja, I.A. Mir, D. Kumar and Rajesh, Biomaterials, 28 (2007), 791.

[4] S. Palaniappan, A.C. Ford, D. Greer, S.M. Everett, D.M. Chalmers, A.T.R. Axon and P.J. Hamlin, Inflamm Bowel Dis I., 13 (2007), 1488.

[5] Y.D. Liu, B.J. Park, Y.H. Kim and H.J. Choi, J. Mater. Chem., 21 (2011), 17396.

[6] R. Mezzenga, J. Ruokolainen, G. H. Fredrickson, E. J. Kramer, D. Moses, A. J. Heeger and O. Ikkala, Science, 299 (2003), 1872.

[7] P.K. Ivanova-Mitseva, V. Fragkou, D. Lakshmi, M. J. Whitcombe, F. Davis, A. Guerreiro, J. A. Crayston, D. K. Ivanova, P. A. Mitsev, E. V. Piletska and S. A. Piletsky, Macromolecules, 44 (2011), 1856.

[8] J.K. Koh, J. Kim, B. Kim, J. H. Kim and E. Kim, Adv. Mater., **23 (**2011), 1641.

[9] I. Sapurina and J. Stejskal, Polym Int, 57 (2008), 1295.

[10] L. Zhang and M. Wan, Adv. Funct. Mater., 13 (2003), 815.

[11] L. Zhang, M. Wan and Y. Wei, Synth. Met., 151 (2005), 1.

[12] Y. H. Huo, H. Zhang, J. Jiang and Y. Yang, J. Mater, J. Mater. Sci., 47 (2012), 7026.

[13] J. Huang and R. Kaner, Pure Appl. Chem., 78 **(**2006), 15.

[14] Q. Sun and Y. Deng, Eur. Polym. J., 48 (2008), 3402.

[15] M. Bai, Y. Cheng, S.A. Wickline and Y. Xia, Small, 5 (2009), 1747.

[16] H.D. Tran, L. Dan and R.B. Kaner, Adv. Mater., 21 (2009), 1487.

[17] C. Luo, H. Peng, L. Zhang, G. Lu, Y. Wang and J. Travas-Sejdic, Macromolecules, 44 (2011), 6899.

[18] M. Trchová and J. Stejskal, Pure Appl. Chem., 83 (2011), 1803.

[19] Y.F. Wang, X.W. Yang, L. Qiu and D. Li, Energy Environ. Sci, 6 **(**2013), 477.

[20] R. Gref, Y. Minamitake, M. T. Peracchia, V. Trubetskoy, V. Torchilin and R. Langer, Science, 263 (1994), 1600.

[21] K.B. Thurmond, T. Kowlewski and K.L. Wooley, J. Am. Chem. Soc., 119 (1997), 6656.

[22] F. Caruso, R.A. Caruso and H. Mohwald, Science, 282 (1998), 1111.

[23] I. Gill and A. Ballesteros, J. Am. Chem. Soc., 120 (1998), 8587.

[24] S. M. Marinakos, J. P. Novak, L.C. Brousseau III, A.B. House, E.M. Edeki, J.C Feldhaus and D.L. Feldheim, J. Am. Chem. Soc., 121 (1999), 8518.

[25] Y. Xia, B. Gates, Y. Yin and Y. Lu, Adv Mater., 12 (2000), 693.

[26] F. Caruso, M. Spasova, V. S. Maceira and M.L. Marzan, Adv. Mater., 13 (2001), 1090.

[27] K. Saralidze, L.H. Koole and M.L.W. Knetsch, Mater., 3 (2010), 3537.

[28] S. Xu, Z. Nie, M. Seo, P. Lewis, E. Kumacheva, H.A. Stone, P. Garstecki, D.B. Weibel, I. Gitlin and G.M. Whitesides, Angew. Chem., 44 (2005), 724.

[29] Y. Xia and G.M. Whitesides, Angew Chem Int Ed Engl., 37 (1998), 550.

[30] Y. Cao, P. Smith and A.J. Heeger, Synth. Met., 48 (1992), 91.

[31] D. Ljerka, M. Karljic and S. Grigic, J. Polym. Sci., 42 (2003), 1599.

[32] J. Huang and R. B. Kaner, J. Am. Chem. Soc., 126 (2004), 851.

[33] H.D. Tran and R.B. Kaner, Chem. Commun., 37 (2006), 3915.

[34] H.D. Tran, I. Norris, J.M. D'Arcy, H. Tsang, Y. Wang, B.R. Mattes and R.B. Kaner, Macromolecules, 41 (2008), 7405.

[35] D. Qin, Y. Xia, G. M. Whitesides. Nat. Protoc., 5 (2010), 491.

[36] J. Stejskal, and R. Gilbert, I.U.P.A.C., Tech. Rep., 74 (2002), 857.

[37] M.K. Ram, O. Yavuz, V. Lahsangah and M. Aldissi, Sens. Actuat. B, 106 (2005), 750.

[38] A.G. Macdiarmid, and A.J. Epstein, Synth. Met., 65 (1994), 103.

[39] B.J. Kim, S.G. Oh, M.G. Han and S.S. Im, Synth. Met., 122 (2001), 297.

[40] E. Detsri and S.T. Dubas, J. Appl. Polym. Sci., 128 (2009), 558.

[41] M. B. Heaney, in The Measurement, Instrumentation and Sensors Handbook (Ed: J.G. Webster), CRC Press, 1999, Ch 43.

[42] Y. Long, Z. Chen, Y. Ma, Z. Zhang, A. Jin, C. Gu, L. Zhang, Z. Wei and M. Wan, Appl. Phys. Lett., 84 (2004), 2205.

[43] Y. Wang, Q. Chen and X. Zeng, Biosens. Bioelectron., 25 (2011), 1356.

[44] Z. H. Wang, C. Li, A. J. Epstein, E. M. Scherr and A. G. MacDiarmid, Phys. Rev. Lett., 66 (1991), 1745.

[45] M. Wan, in Conducting Polymers with Micro Or Nanometer Structure, 1st ed. Springer, Tsinghua University Press, Beijing, 2008, Ch 5.

[46] X. Zhang, J Colloid Interface Sci, 212 (1999), 107.

[47] Y. Tan and A.P. Lee, Lab Chip, 5 (2005), 1178.

[48] D.C. Trivedi. In: Nalwa HS, editor. 1997. Handbook of organic conductive molecules and polymers, vol. 2. Chichester (UK): Wiley, Chapter 12.

[49] J. Prokes, M. Trchova, D. Hlavata and J. Stejskal, Polym. Degrad. Stab., 78 (2002), 393.

Chapter 3
Encapsulation of Glucose Oxidase in Polyaniline Microspheres for Glucose Sensing

3.1 Introduction

Biosensors are widely applied to many fields such as biocatalytic processes, medical care, food, environment, industries, security and defense [1-3]. Enzyme-based biosensors are an important analytical tool as enzymes have the unique ability of quickly and accurately recognizing target molecules in a complex system. Since the initial development of the first enzyme sensor [4], tremendous effort has been directed towards research into glucose enzyme biosensors because of their great promise in a vast range of application fields such as medical diagnostics, diabetes management, bioprocess monitoring, the beverage industry, and environmental monitoring [5-13]. Electrochemical glucose sensors are widely used due to their low-cost, fast time-response and simple operation procedures. For amperometric glucose sensors, glucose oxidase (GOx) is the most commonly used enzyme for the specific recognition of glucose. In the presence of molecular oxygen, immobilized GOx catalyzes the oxidation of glucose to gluconolactone, and generates hydrogen peroxide as a byproduct, where two protons and two electrons are released during the reaction [14].

$$\text{Glucose} + O_2 \xrightarrow{\text{GOx at 0.4 V}} \text{Gluconic Acid} + H_2O_2 \quad (3.1)$$

$$H_2O_2 \xrightarrow{0.4\,V} O_2 + 2H^+ + 2e^- \quad (3.2)$$

The immobilization of GOx has been accomplished by using host matrices such as polymers [14-19] and carbon based materials [20-26]. Most of the studies reported the use of composite materials to immobilize GOx to amplify the signal, which is expensive, and the immobilization procedure is complicated.

Immobilization of enzymes in conducting polymers has many advantages such as efficient transfer of electric charge without an external mediator [27], considerable flexibility in available chemical structure [28], and the rather high stability of conducting polymers themselves. Polyaniline (PANI), being conducting, can enhance the measurable response and make it possible to detect low concentrations of the substrate while eliminating the need for external mediators to amplify the signal. Immobilization of enzymes in conducting polymers to form biosensors has been made mainly by one-step process [29] or two-step process [30-33]. In the one-step process, an enzyme was entrapped into a polymer film directly during electrochemical polymerization of aniline. The one-step process is simple and cheap, but parts of GOx affected by monomers of aniline were denatured and inactive [32]. In the two-step process, on the other hand, GOx was introduced during the oxidation stage of the reduced PANI in a buffer solution containing active GOx. This prevents the denaturation of GOx during the polymerization process but it affected the stability of GOx as it was adsorbed onto the surface of the PANI film [33]. A template process to immobilize GOx in PANI was able to overcome the issue of stability but it required a three-step process to achieve the immobilization. [34].

In this study, a facile, one-step and low cost microfluidics technique for the immobilization of GOx in PANI microspheres which will retain the activity of GOx is investigated. The specific objectives are listed below.

1. Encapsulate glucose oxidase in polyaniline microspheres using a T-junciton microfluidic device discussed in the previous chapter.
2. Investigate the capability of glucose sensing of long term stability of GOx encapsulated PANI particles.

3.2 Materials and Methods

3.2.1 Materials

Slygard 184 silicone elastomers kits (polydimethylsiloxane, PDMS, and curing agent) were purchased from Dow Corning Co (Midland, MI). SU-8 2035 photoresist, 4 inch silicon wafers, peroxide-cured silicon tubing (ID 0.76 mm, Cole Palmer), BD plastic syringes of 1 ml volume, 26 gauge Sub-Q luer lock needles, 0.38 mm ID polyethylene tubing and multiple syringe pumps from Harvard Apparatus were used. Ammonium persulfate (APS), Aniline (Ani), 1-4 phenylenediame (p-PDA) and Span 85 were used as received from Sigma-Aldrich without further purification. Deionized water and hexadecane were used as the phase solvents. Type II-S glucose oxidase (GOx) from Aspergillus niger (EC 1.1.3.4) was purchased from Sigma-Aldrich (St. Louis, MO). Enzyme stock solutions were prepared in 5 mL of potassium phosphate buffer (0.05 M, pH 7) in DI-water. Glucose solutions (1 – 30 mM) were prepared from a pure substrate, dissolved in potassium phosphate buffer solutions (pH 7) and equilibrated at room temperature before the experiments for mutarotation. APS (0.4M) was prepared in DI-water. The oxidizing agent, ammonium per sulfate (APS), was mixed with GOx for 1 hour at room temperature. Unlike the solution used in Chapter 2, hydrochloric acid (HCl) was not added to APS as GOx is only active in the pH range 4 – 7 and might be denatured below pH 4. The pH of the current APS and GOx aliquot is 5.5. The final concentration of GOx in the APS solution was 1 U/ μL. The same microfluidic device as described in Chapter 2 was used. The micro-devices were fabricated using standard photo and soft lithography techniques. A syringe pump (Harvard apparatus) was used to pump the APS and GOx aliquot and aniline into the device through the inserted

polyethylene tubing (Intramedic). The PDMS-glass microfluidic device has been described in detail in Chapter 2.

3.2.2 Experimental setup

Aniline (0.2 M) and APS (0.4 M) containing GOx (1 U/ µL) were pumped through the microchannels. A similar procedure as described in Chapter 2 was performed to form the polyaniline (PANI) microspheres. However, in this case, the GOx present in the APS droplets is immobilized inside during the formation of the PANI network during polymerization. The polyaniline microspheres are collected off chip in a water solution, pH 7, and separated from the continuous oil phase.

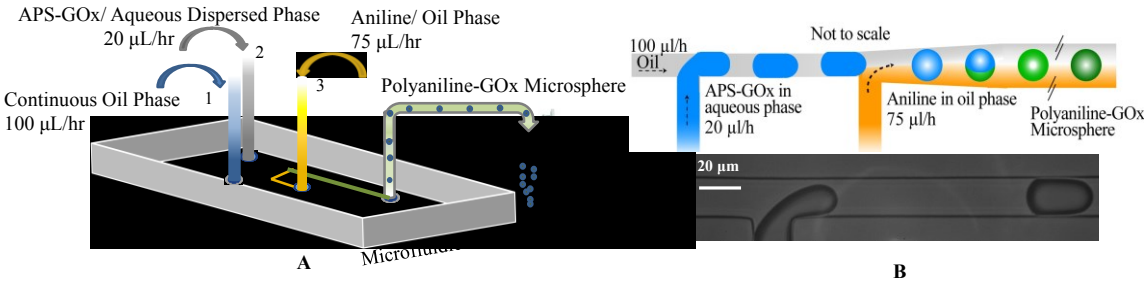

Figure 3.1. (A) Polyaniline droplets encapsulating glucose oxidase were produced in a T-junction microfluidic device containing two continuous phases, aniline and hexadecane, and one dispersed phase, APS with GOx. The polymerized aniline droplets were transported off-chip through an exit.

The PANI microspheres encapsulating GOx are used to sense glucose solution. An aliquot of 5 µL of polyaniline microspheres encapsulating GOx is deposited on the working part of a gold electrode. To maximize sensitivity of the sensor and lower the variability, a PDMS well was placed on the gold electrode covering a part of the gap between the electrodes and the

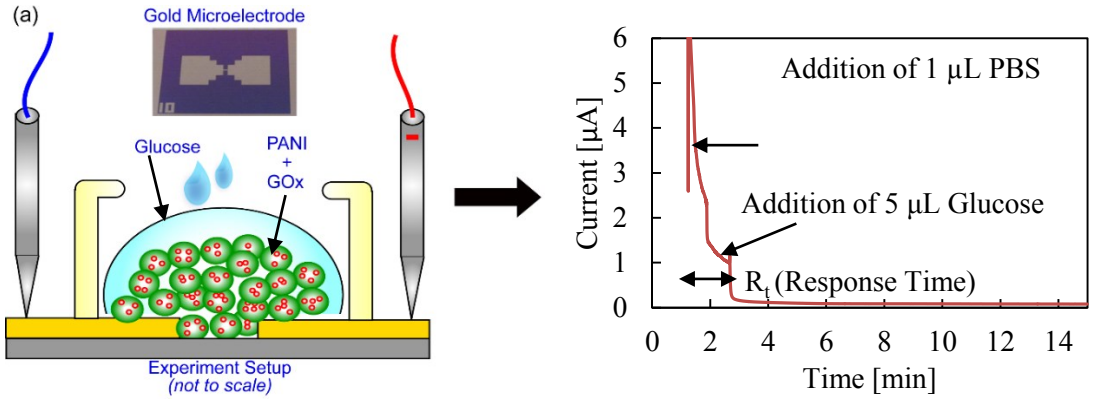

Figure 3.2. (a) Experimental setup used to perform chronoamperometry studies. (b) Representative chronoamperometry response observed in the PANI-GOx structure for all the glucose concentration tested. The plot showed the response of the PANI-GOx at 5 mM glucose.

microspheres were then deposited on the electrode. The aliquot is dispersed in water which is allowed to evaporate at room temperature resulting in a film of dry PANI- GOx microspheres on the electrode. 1 µL of potassium phosphate buffer is deposited over the entire surface of the electrode to stabilize the dry PANI-GOx microspheres. After 1 minute, 5 µL of glucose solution of known concentration is deposited over the entire surface of the electrode in the PDMS well. The chronoamperometry response (0 – 15 minutes with applied voltage of 0.4 volts) of the PANI-GOx microspheres under different glucose concentrations (1 – 30 mM) is recorded. The detection of glucose was determined by measuring the anodic potential oxidation of hydrogen peroxide produced in the reactions given by the below reaction and the current released is measured for 15 minutes using the picometer.

3.2.3 Material Characterization

Morphologies of the PANI-GOx microspheres were observed using a field emission scanning electron microscope (SEM, FEI Sirion) with an acceleration voltage of 5 kV. 2 µL of the PANI-GOx microspheres aqueous dispersion was deposited on a carbon/formvar TEM grid (Ted Pella Inc, CA) and air dried at room temperature.

Ultraviolet – visible (UV-Vis) spectrometry was performed at 25 °C using a Varian Cary 5000 UV – Vis – NIR Spectrophotometer coupled with a temperature controller. 5 µL of the PANI-GOx microspheres aqueous dispersion was deposited on a glass slide and dried at room temperature for an hour before performing UV-Vis spectrometry.

For glucose sensing a microfabricated gold electrode with 10 µm in gap size and a Keithley 6485 picometer were used to obtain the average current in the PANI-GOx microspheres. All shown results were from one day-old samples unless specified otherwise.

3.3 Results

3.3.1 Morphology of Polyaniline-GOx

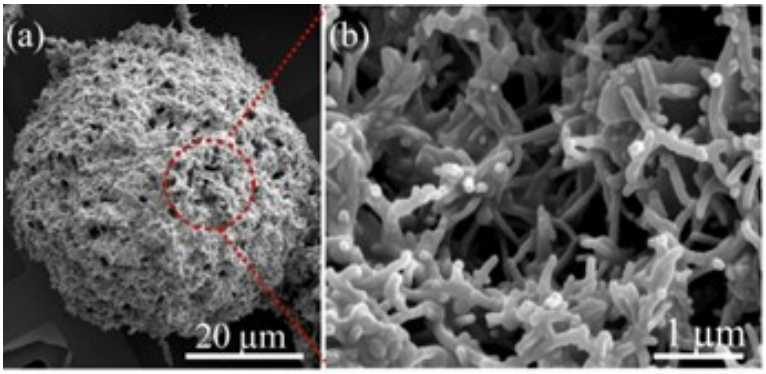

Figure 3.3. SEM images of a 0.2 M (APS/Aniline = 2:1) PANI-GOx microsphere 2 hours after fabrication in the present study are shown above. The PANI-GOx microsphere has a porous structure with a polymerized aniline outer layer. (b) A magnified image of the microsphere shows the porous morphology.

The morphology of the PANI-GOx microsphere was similar to PANI microspheres without GOx. The dried microspheres were stored at room temperature (25°C) and exposed to air. Emeraldine salt form of PANI is green in color and its base form is blue. After complete polymerization, all PANI microspheres are green in color, indicating their emeraldine salt form. They were approximately 50 µm in diameter with a porous polymerized PANI outer layer, which consists of fibril structures of diameters 200 – 500 nm, as in Figure 3.3 (b). The layer contains pores between 300 nm - 1µm and fibrils of diameter ~150 nm, distributed at random orientations. The rate of polymerization was enhanced by the addition of initiator p-PDA as it accelerated the polymerization rate which favored homogenous nucleation over heterogeneous nucleation.

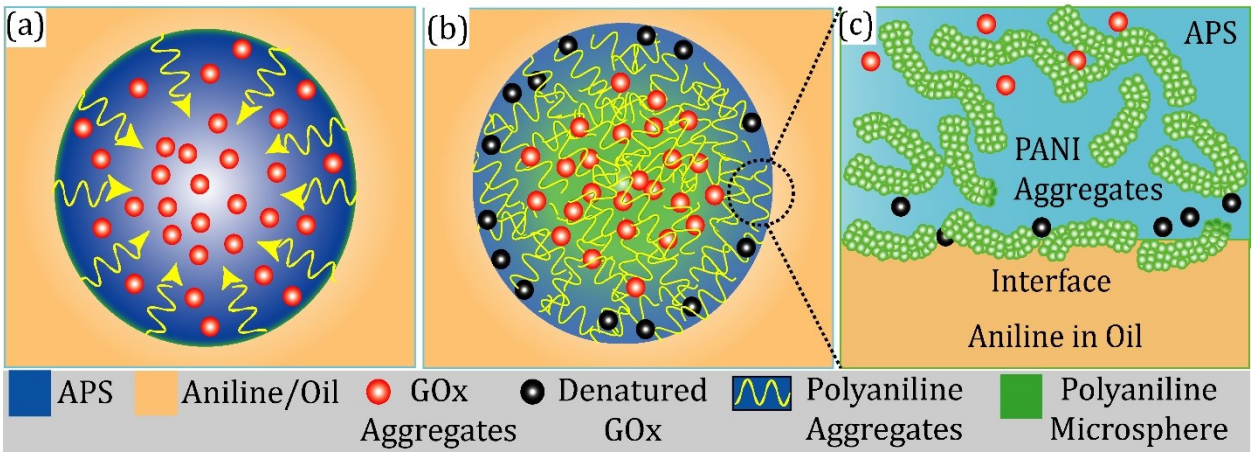

Figure 3.4. Schematic of GOx encapsulation inside the polyaniline microspheres is shown. (a) Aniline (in orange) interacts with APS (in blue) – GOx (in red) droplet at the interface and forms polyaniline nanostructures (in yellow). Polyaniline being hydrophilic diffuses into the APS-GOx droplet and starts aggregating inside the droplet. (b) Polyaniline aggregates form interlinked layers and physically entrap the GOx aggregates leading to the formation of a microsphere. (c) Polyaniline nanostructures formed at the interface of the aqueous and oil phase diffuse into the aqueous phase. The GOx aggregates present at the interface of APS/ Aniline are denatured during the polymerization process while those away from the interface are protected and remain active.

We hypothesize that the PANI nanostructures that are formed at the interface of the aniline/ APS droplet migrate toward the hydrophilic environment within the APS droplet. The PANI nanostructures aggregate within the APS droplet and physically trap the GOx within their structure (Figure 3.4). GOx is hydrophilic and prefers to stay within the APS droplet. Previous PANI/ GOx immobilization techniques reported the denaturation of all the GOx during the polymerization process. We speculate that in the above microfluidic process, the GOx aggregates that remain within the APS droplet are not denatured and retain the activity. However, the GOx aggregates that are at the interface APS/ Aniline droplet will be denatured during the interfacial

polymerization process. The active GOx within the APS droplet can be verified indirectly by the spectroscopic response and chronoamperometry during the glucose sensing.

3.3.2 UV-Vis Spectrometry

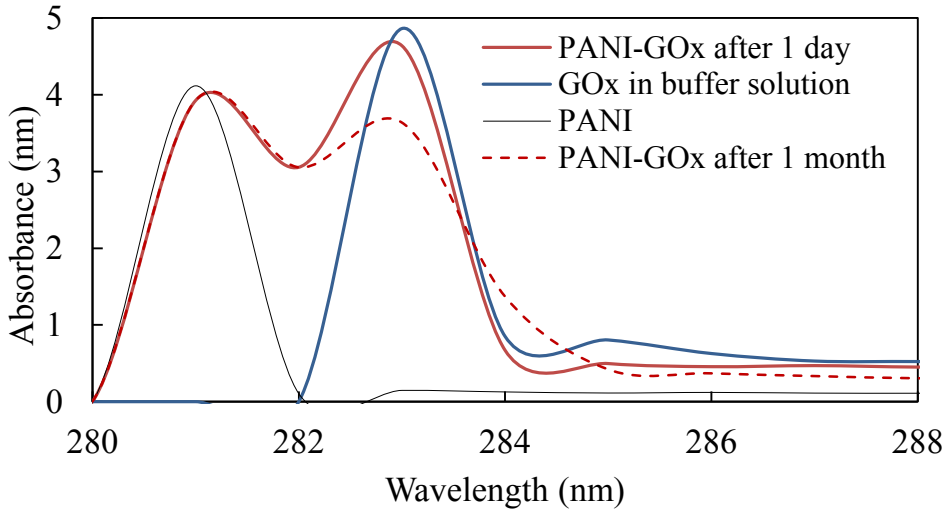

Figure 3.5. UV-Vis absorbance spectrum of the PANI microspheres encapsulating GOx after 1 day and 1 month are shown and compared with plain PANI microspheres.

UV – Vis spectrometry was performed to verify the encapsulation of GOx within the PANI microspheres. In Figure 3.5, plain PANI microspheres showed a peak (black curve) at 281 nm. Characteristic resonance peaks of GOx in a buffer solution occurred at ~283 nm (blue curve) consistent with values reported in literature [34]. For the PANI-GOx microspheres, similar resonance peaks were observed (red curve) indicating that the bulk of GOx was not denatured during the immobilization process. Similar resonance peaks were also observed in ~ 1 month old PANI-GOx microspheres stored at room temperature after air drying, demonstrating good stability of GOx inside the PANI microspheres. GOx is active within the pH range of 4 – 7. The pH value of the PANI microspheres was measured to be ~ 5.5 ± 0.1.

3.3.3 Chronoamperometry

Calibration curves for current released versus glucose concentration for fresh PANI-GOx microspheres (1 day old) and PANI microspheres were obtained (Figure 3.6). PANI-GOx microspheres exhibited a linear response over a wide range of the glucose concentration, 1 – 30 mM. The control was plain PANI microspheres which exhibited a near constant current output over the glucose concentration range used for sensing. However, the current response was an order of magnitude lower as compared to the calibration curve of PANI-GOx microspheres between glucose concentrations 5 mM – 30 mM. The amperometric response is higher than that reported by Pan et al. [35] where GOx was immobilized in a PANI film matrix in a 2 step process. Note that very low volumes of PANI-GOx microspheres (~ 5 μL) were able to produce amperometric response in the range of micro amperes.

The stability of the PANI-GOx sensor was tested every 5 days over a month (Figure 3.7). Electrodes containing the PANI-GOx microspheres film were stored in vacuum at 4 ºC during this period. The amperometric response decreased by 35% after 30 days. The reason could be the lack of an aqueous environment, which is critical to maintain the activity of GOx.

Our ongoing effort is to improve the stability by storing the PANI-GOx spheres in a buffer solution to preserve the activity of the enzyme. A limitation of the microfluidic method is the lack of knowledge of the exact amount of GOx in each microsphere. This led to variability in the current output from sample to sample. However, the variability was not significant.

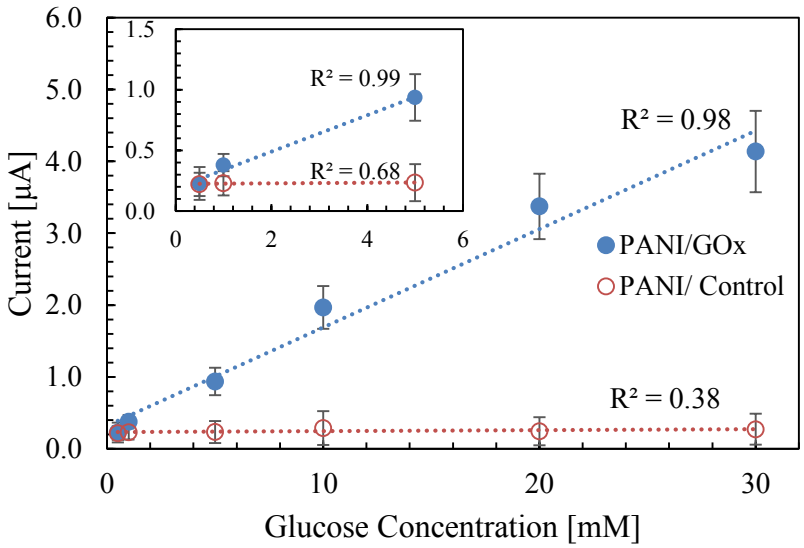

Figure 3.6. Amperometric response of a day old PANI-GOx microspheres and a day old PANI microspheres at different glucose concentrations. Linear response with high correlation coefficient (R^2) was observed in the PANI-GOx microspheres. The inset, magnified part of the area in the red box, shows the linear response at the lower concentrations of glucose. The activity of the glucose oxidase encapsulated is 1 U/µL.

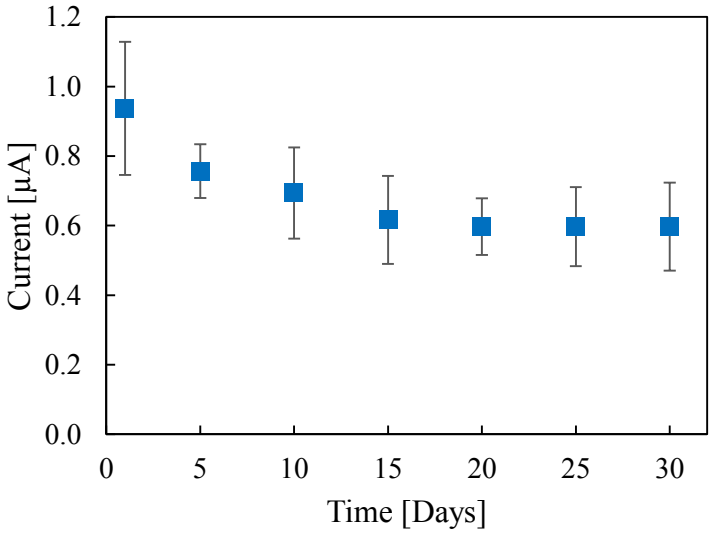

Figure 3.7. The stability of the PANI-GOx microspheres stored in vacuum at 4 ºC over 30 days is shown. The amperometric response at 5 mM glucose concentration lowered by 35% after a month.

3.3.4 Substrate Kinetics

The relationship between the substrate concentration and the reaction rate may be described by the Michaelis-Menten equation:

$$v_{\mathrm{o}} = v_{max}\mathrm{S}/(\mathrm{K_m} + \mathrm{S}) \quad (3.3)$$

where v_o is the initial rate of reaction, v_{max} is the maximum rate of reaction, S is the solution concentration and $\mathrm{K_m}$ is the Michaelist-Menten constant. The $\mathrm{K_m}$ value characterizes the affinity between the substrate and the enzyme. A low $\mathrm{K_m}$ value reflects high affinity. At low substrate concentrations ($\mathrm{S} \ll \mathrm{K_m}$), the reaction rate is directly proproportional to the substrate concentration ($\mathrm{S} \gg \mathrm{K_m}$), the reaction is zero-order and no longer dependent on the substrate concentration but is only dependent on the enzyme activity. $\mathrm{K_m}$ can be calculated from the Lineweaver-Burke plot (Figure 3.8). A Lineweaver-Burke plot contains reciprocal values of $\mathrm{v_o}$ and S on the y and x axes, respectively. In ampermetric responses, v_o can be represented by the current output, I. The Lineweaver-Burke equation is as follows:

$$1/\mathrm{I} = 1/\mathrm{I_{max}}\,(1 + \mathrm{K_m}/\mathrm{S}) \quad (3.4)$$

The apparent Michaelis–Menten constant (K_m) was calculated for the immobilized enzyme by an amperometric method as suggested by Shu and Wilson [36]. The plots of current inverse against glucose concentration inverse are shown in Figure 3.8. The maximum current response I_{max} and the apparent Michaelis–Menten constant K_m can be calculated from the intercept and the slope. The maximum current response I_{max} was 2.86 μA, with K_m = 5.97 mM. The value of K_m was lower than the reported value 19.6 mM in literature [32]. According to the character of Michaelis–Menten constant (K_m), the smaller the value of K_m, the stronger the affinity between the enzyme and the substrate [37]. So the affinity between glucose and GOx in

the PANI-GOx sensor prepared by the one-step droplet microfluidic process is stronger than those reported in previous studies. A strong affinity ensures that the GOx can catalyze the reaction even at low concentrations of glucose solution.

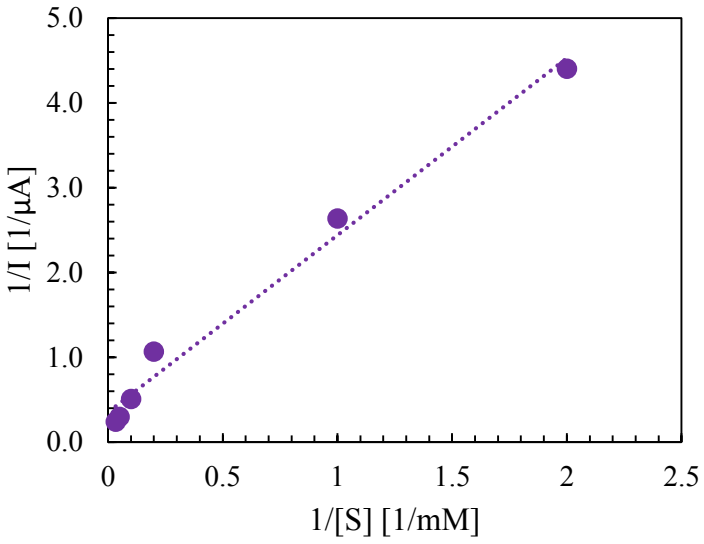

Figure 3.8. Lineweaver-Burke plot for GOx immobilized in PANI microspheres is shown. The slope is calculated to be 2.09 mM/μA and the y intercept is 0.35 μA^{-1}.

The use of our droplet microfluidic technique used to fabricate PANI-GOx microspheres eliminates the need for mediators to amplify the signal and protects GOx from denaturing during the polymerization process which has been the bottle neck in previous studies. Further, the pH range under which PANI can be fabricated (pH 1.5 – 6) can also be used to encapsulate other types of enzymes active at a lower pH range.

3.4 Conclusion

We used a facile one-step and cost-effective droplet microfluidic process to immobilize GOx in PANI microspheres. The water in oil emulsion microfluidic technique protected the GOx from being denatured during the polymerization process at the interface of the APS droplet and aniline and maintained its activity. The PANI-GOx sensor had a linear amperometric response over a wide range of glucose concentrations, 1 – 30 mM, with a response in the micro ampere range at lower concentrations, 1 – 5 mM. The Michaelis–Menten constant (K_m) is 5.97 mM which indicates better affinity between GOx and glucose than earlier reported PANI-GOx sensors. A stronger affinity of the PANI-GOx sensor ensures that the sensor can work even when low concentrations of glucose is used. The activity of PANI-GOx was lowered by 35% after a month when it was stored in vacuum at 4 ºC. The stability can be improved by storing the PANI-GOx sensor in a buffer solution. This work is in progress. Nevertheless, the amperometric performance of the PANI-GOx sensor shows great promise and eliminates the need for mediators and tedious procedure in a conducting polymer to maintain the enzyme activity.

References

[1] S. J. Alcock and A.P.F. Turner, (1994), 319.

[2] M. J. Dennison and A.P.F. Turner, 139 (1995), 1.

[3] E. Kress-Rogers, 1996. Boca Raton, USA: CRC Press.

[4] L. C. Clark Jr. and C. Lyons, *Ann. N. Y. Acad. Sci.* 102 (1962), 29.

[5] J. Wang, Chem. Rev. 108 (2008), 814.

[6] J. D. Newman, A. P. F. Turner, Biosens. Bioelectron. 20 (2005), 2435.

[7] A. Heller, B. Feldman, Acc. Chem. Res. 43 (2010), 963.

[8] M. Gerard, A. Chaubey, B. D. Malhotra, Biosens. Bioelectron. 17 (2002), 345.

[9] C. Dhand, M. Das, M. Datta, B. D. Malhotra, Biosens. Bioelectron. 26 (2011), 2811.

[10] A. I. Gopalan, K. P. Lee, D. Ragupathy, S. H. Lee, J. W. Lee, Biomaterials 30 (2009), 5999.

[11] H. G. Xue, Z. Q. Shen, C. M. Li, Biosens. Bioelectron. 20 (2005), 2330.

[12] A. Kausaite-Minkstimiene, V. Mazeiko, A. Ramanaviciene, A. Ramanavicius, Biosens. Bioelectron. 26 (2010), 790.

[13] Y. Xian, Z.; Hu, Y.; Liu, F.; Xian, Y.; Wang, H. T.; Jin, L. T.Glucose, Biosens. Bioelectron. 21 (2006), 1996.

[14] P. Lin and F. Yan, Adv. Mater., 24 (2012), 34.

[15] A. Kros, S. W. F. M. van Hovell, N. A. J. M. Sommerdijk and R. J. M. Nolte, Adv. Mater., 13 (2001) 1555.

[16] Y. Yang, C. Yi, J. Luo, R. Liu, J. Liu, J. Jiang and X. Liu, Biosens. Bioelectron., 26 (2011), 2607.

[17] P. D. Gaikwad, D. J. Shirale, V. K. Gade, P. A. Savale, J. J. Kharat, K. P. Kakde and M. D. Shirsat, Int. J. Electrochem. Sci., 1 (2006), 425.

[18] J. Liu, M. Agarwal and K. Varahramyan, Sens. Actuators, B, 135 (2008), 195.

[19] M. Hiller, C. Kranz, J. Huber, P. Bauerle and W. Schuhmann, Adv. Mater., 8 (1996), 219.

[20] F. Gutierrez, M. D. Rubianes and G. A. Rivas, Sens. Actuators, B, 161 (2012), 191.

[21] X. Wang and S. Uchiyama, Anal. Lett., 41 (2008), 1173.

[22] P. Rai, T. Ho, J. Xie, J. A. Hestekin and V. K. Varadan, J. Nanotechnol. Eng. Med., 1 (2010), 021009.

[23] H. R. Luckarift, D. Ivnitski, R. Rincon, P. Atanassov and G. R. Johnson, Electroanalysis, 22 (2010), 784.

[24] G. Palestino, R. Legros, V. Agarwal and C. G. E. Perez, Sens. Actuators, B, 135 (2008), 27.

[25] K. Zhou, Y. Zhu, X. Yang and C. Li, Electroanalysis, 22 (2010), 259.
[26] D. Lee, J. K. J. Lee, J. Kim, H. B. Nab, B. Kim, H. S. C. Kwak, A. Dohnalkova, J. W. Grate, T. Hyeon and K. H. S, Adv. Mater., 17 (2005), 2828.
[27] P. De Taxis du Poet, S. Miyamoto, T. Murakami, J. Kimura, I. Karube, Anal. Chim. Acta 235 (1990), 255.
[28] M. Gerard, A. Chaubey, B.D. Malhotra, Biosens. Bioelectron 17 (2002), 345.
[29] D. Belanger, J. Nadream, G. Fortier, J. Electroanal. Chem, 274 (1989), 143.
[30] M. Umana, Waller, J. Anal. Chem. 58 (1986) 2979.
[31] N.C. Foulds, C.R. Lowe, J. Chem. Soc., Faraday Trans. I, 82 (1986), 1259.
[32] S. Mu, H. Xue, B. Qian, J. Electroanal. Chem, 304 (1991), 7.
[33] J. Kan, S. Mu, H. Xue, H. Chen, Synth. Met, 87 (1997), 3.
[34] K. Shin, H. Youn, Y. Han, S. Kang, Y. Hah, Eur. J. Biochem. 215 (1993) 747.
[35] X. Pan, J. Kan, L. Yuan, Sensors Actuators B, 102 (2004) 325.
[36] F.R. Shu, G.S. Wilson, Anal. Chem, 48 (1976), 1679.
[37] I.H. Segel, Biochemical Calculations, 2nd ed., Wiley, New York, 1976, p. 152.

Chapter 4

Manipulating particles shapes: Deformation of immiscible viscoelastic molten wax drops at a liquid interface

4.1 Introduction

Non-spherical shaped particles are of great potential for use in biotechnology [1], cosmetics [2], structural materials [3], and pharmaceuticals [4]. They are highly desired as the non-spherical shape can offer unique properties such as high packing density [5], large surface areas, enhanced properties like intrinsic viscosity which is dependent on the orientation of the particle [6] and anisotropic responses to external electric and magnetic fields [7-9], when compared with those of spherical particles. Extensive research has been reported on the synthesis of non-spherical polymeric particles using microfluidics and self-assembly ranging in sizes from microns to millimeters [10-14]. The primary limitation is the type of shapes each method can produce and the requirement of specialized equipment. Recently, non-spherical particle fabrication by impinging and deforming alginate microgel drops on liquid substrates and crosslinking in a bulk medium has been reported [15, 16]. This technique holds great promise as it is simple, low cost and can be used for large scale manufacturing of particles. Also, liquid drop impact and subsequent deformation on surfaces is of fundamental importance due to its application in a wealth of areas including inkjet printing [17, 18], food processing, spray coating in the consumer goods and pharmaceutical industries [19, 20], delivery of drugs and agrochemicals, optical

sensing, soil erosion due to rain [21] and turbine wear. Most liquid drop impact in a liquid medium studies have been performed applying chemical crosslinking [15, 16]. However, there is a gap in knowledge of liquid drop impact utilizing thermal effects to generate particles. This motivates the study of liquid drop impact in a liquid medium involving thermal solidification to generate and control the particle shape.

Shaped particles can be produced by the deformation and solidification of molten drops in an immiscible cooling medium. Previous research efforts have been primarily directed on the impact of molten metal or paraffin wax drops on a solid surface which either generated irregular discs on solidification or the drops recoiled after impact and broke up into satellite drops [22-26]. Numerical models have also been developed to predict the effect of varying process variables on the final product for drop impact on solid substrate [22]. However, the interfacial dynamics associated with impinging molten drops on liquid surfaces and the subsequent solidification is complex and not understood in detail. Also, a moving phase interface provides more freedom during the deformation and solidification of the molten drop when compared with a solid surface.

This work aims to examine the deformation and solidification of millimeter size, viscoelastic molten wax drops at an immiscible liquid interface that produces non-spherical particles. Viscoelastic wax based materials are widely used in many applications: dentistry [27], consumer goods [28], food processing [29] and drug delivery [30]. Their performance and application depends on the particle morphology and size. The secondary objective is to develop a capability of predicting the final shape as affected by the process parameters using experimental results and a simplified mathematical model.

In this study, a model wax system described previously by Pawar et al. [31] is used. The deformation process of the molten wax drop is observed using high speed imaging under conditions of varying viscous, interfacial, inertial and thermal forces. The shear viscosity of the bath fluid and the interfacial tension between wax and bath is varied by the addition of glycerol and surfactant. Dimensionless numbers can be used to describe the behavior during impact such as Weber, Reynolds, Capillary and Stefan numbers which compare the relative importance of inertial, viscous, interfacial and thermal forces. The parameters are defined as follows.

$$\mathrm{We} = \frac{\rho_w U_o^2 (2R)}{\sigma_{w/f}} = \frac{\text{Inertial Force}}{\text{Interfacial Force}} \tag{4.1}$$

$$\mathrm{Ca} = \frac{\mu_f U_o}{\sigma_{w/f}} = \frac{\text{Viscous Force}}{\text{Interfacial Tension}} \tag{4.2}$$

$$\mathrm{Re} = \frac{\rho_f U_o (2R)}{\mu_f} = \frac{\text{Inertial Force}}{\text{Viscous Force}} \tag{4.3}$$

$$\mathrm{St} = \frac{C_p \Delta T}{L_w} = \frac{\text{Sensible Heat}}{\text{Latent Heat}} \tag{4.4}$$

where ρ_w, R, U_o, $\sigma_{w/f}$, μ_f, ρ_f, C_P, ΔT, L_w denote the density and radius of wax drop, impact speed, interfacial tension between the molten wax and the bath liquid, viscosity of bath, density and specific heat of bath, temperature difference between bath and wax and latent heat of wax respectively. The subscript f denotes the bath fluid property while w denotes wax property. Cursory phase diagrams using the dimensionless numbers will be produced with the objective of developing a capability to predict the final morphology of the wax particles as affected by the initial process conditions. A simplified mathematical model will be solved to correlate the final morphology of the wax particles and its phase transition region.

4.2 Materials and Methods

4.2.1 Materials

Vaseline, hexadecane, glycerol and sodium dodecyl sulfate (SDS) were purchased from Sigma-Aldrich (St. Louis, MO) and used without further processing. Deionized water was used for preparing the bath fluids. BD plastic syringes of 1 ml volume, 26 and 18 gauge sub-Q luer lock needles and syringe pumps from Harvard Apparatus were used for extruding molten wax drops. The drop sample was prepared by mixing 70% Vaseline and 30% hexadecane by weight in a vortex mixer for one minute and stored at room temperature. Three different fluids were used as the bath fluid: water, water containing 0.025% w/w SDS and water containing 30% w/w Glycerol. The properties of all three fluids are given in Table 4.1.

Table 4.1. Properties of the Bath Fluids at Room Temperature

Fluid	Density (kg/m^3)	Surface Tension (mN/m)	Viscosity (mPa.s)
Water	997.69	72.6	0.969
Water 0.025% w/w SDS	997.94	51.1	0.969
Water 30% w/w Glycerol	1077.5	64.5	2.357

4.2.2 Material Characterization

4.2.2.1 Bulk Shear Rheometry

Vaseline is a petroleum wax consisting of mineral oil and crystalline hydrocarbons and is immiscible within an aqueous solution. The sample mixture, 70% Vaseline and 30% hexadecane by weight, changes phase from a solid to a liquid when heated and the phase transition

temperature can be determined from calorimetry techniques as well as temperature dependent rheometry.

Steady shear rheometry and oscillatory shear rheometry were performed within a temperature range 25 – 75 ºC using a stress-controlled rheometer (AR 2000, TA instruments). An aluminum cone-plate geometry (60 mm in diameter and 1º truncation angle) was used for all measurements. The temperature was regulated by a Peltier temperature controller and a solvent trap was used to prevent heat loss to the atmosphere. Figure 4.1a shows the shear viscosity of the sample as a function of shear rate at different temperatures. It exhibits shear thinning behavior and the zero shear viscosity decreased with increase in temperature. The shear rates applied in the measurement ranged from 2 and 1000 s^{-1}. Molten wax behaved as a Herschel-Bulkley material due to the presence of a yield stress in the range of 1.3 mPa – 1.7 Pa, which decreased with increasing temperature (Figure 4.1b). This was due to the solid crystals which melted as temperature increased. During cooling, the elastic and viscous modulus values, G' and G", increased with decreasing temperature (Figure 4.1c). As the sample cooled, the wax crystals precipitated and formed an interlocked three-dimensional crystal network [32-34]. The network increased the solid nature of the sample as indicated in the rise in elastic modulus, G'. In the temperature range of 40 – 45 °C, a crossover with G' > G" was observed (Figure 4.1c) which could also be used as a simple criterion for the phase transition region. Phase transition temperature relates to the wax crystallization phenomena and the wax crystal aggregation in clusters leading to solidification. The critical strain above which the sample was dominated by the viscous behavior decreased with increasing temperature (Figure 4.1d). The values of G' and G" measured in the linear viscoelastic regime were found to be independent of frequency during

isothermal oscillatory frequency sweep measurements. The sample will be referred to as molten wax and after solidification as wax in the study.

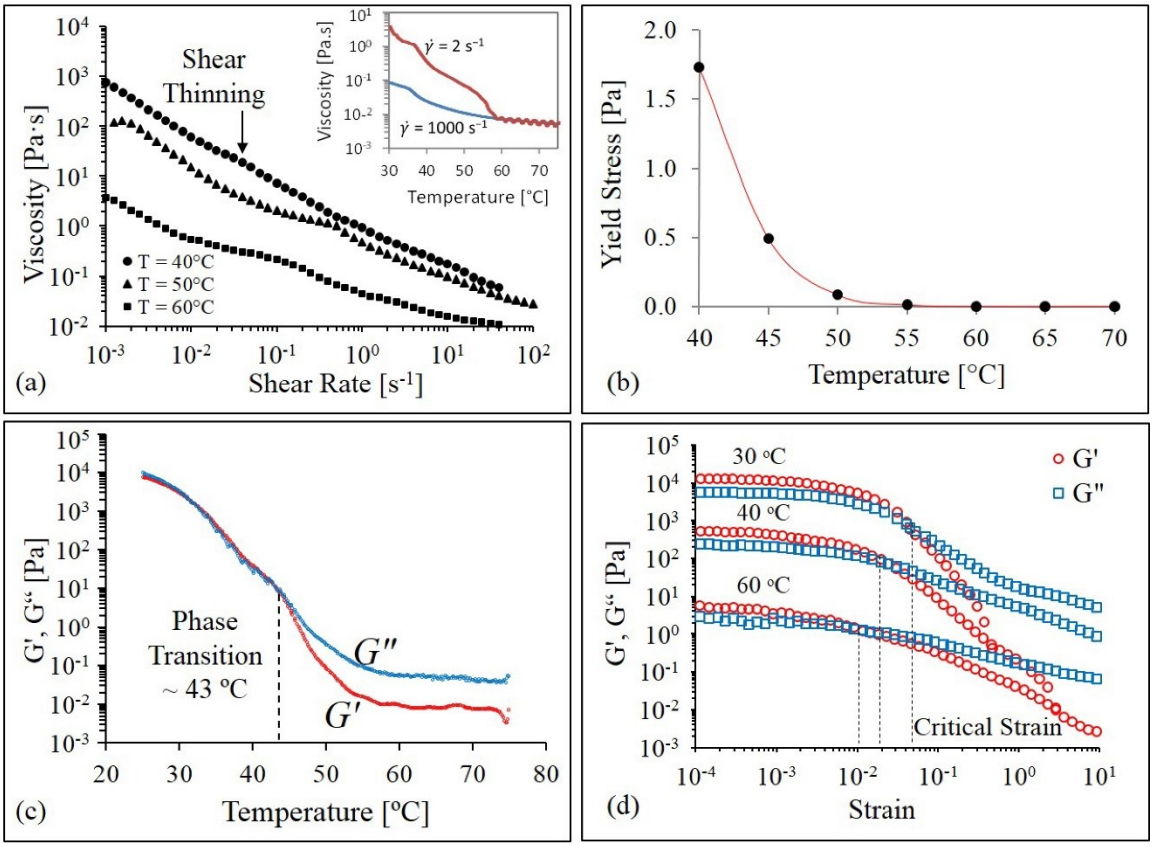

Figure 4.1. (a) Shear viscosity vs. shear rate for the sample at different temperatures. Inset shows the shear viscosity at shear rates 2 s^{-1} and 1000 s^{-1}. (b) Yield stress of the sample at different temperatures. (c) Elastic modulus, G', and viscous modulus, G", are plotted against temperature under 1% strain and 1 Hz frequency. (d) G' and G" vs. strain at different temperatures of wax.

4.2.2.2 Interfacial Tension

The interfacial tension between the molten wax and bath liquid at specific temperatures was measured using a force Tensiometer (Sigma 700, Attension) which can measure surface tension in the range of 1 – 500 mN/m at a resolution of 0.001 mN/m. Molten wax was maintained at temperatures between 40 – 75 ºC and the Wilhelmy plate method was employed at equilibrium. The interfacial tension increased from 6.41 mN/m to 15.48 mN/m with increasing temperature from 40 ºC to 75 ºC of molten wax. The temperature of the bath fluid was the same as that of the molten wax at the interface.

4.2.2.3 Density of Wax

The variation in the wax weight was determined between 38 – 80 ºC at temperature ramp rates of 1 ºC /min and 10 ºC /min using a thermogravimetric analyzer (Discovery TGA, TA Instruments) and found to be negligible. The density of wax was inferred from the weight of a known volume and was measured to be 865 kg/m^3.

4.2.2.4 Thermal Properties of Wax

The heat flow in wax from 20 - 80 ºC was measured by using a differential scanning calorimeter (Auto Q20, TA Instruments) at cooling rates of 10 ºC/min and 1 ºC/min. The heat capacity, thermal conductivity, enthalpy of crystallization and the phase transition temperature of the wax were calculated from the heat flow curves. The thermal properties are listed in Table 4.2. The phase transition temperature determined by calorimetry is initiated approximately 45.93 ºC and is not significantly different from the phase transition temperature region determined from oscillatory shear rheometry, 41 – 45 °C. This indicated that the thermal phenomenon is

correlated to the rheological behavior of wax. The solidification of molten wax occurs over the phase transition temperature region and is not instantaneous.

Table 4.2. Thermal properties of Wax at 10 ºC/min from 40 – 75 ºC

Property	Value
Heat Capacity, C_P (kJ/ kgK)	1.71
Thermal Conductivity, k (W/ mK)	0.15
Enthalpy of Crystallization, L (kJ/ kg)	18.51
Phase Transition Temperature, T_F (ºC)	45.93

4.2.3 Experimental Procedure

A schematic of the experimental setup is shown in Figure 4.2. A high speed camera (Phantom V310, Vision Research Inc.) at 4000 fps was used to visualize the impact of the wax drop at the air-liquid bath interface. The impact was backlit by 24 LED high power source and the diffused light was achieved by using a standard diffusing paper. Molten wax drops were generated using a pressure driven syringe pump at a constant rate. Two different flow rates, 3 µL/min and 1 mL/min and two sizes of the needles, 26 and 18 gauge, generated drops of sizes 1.8 mm and 3.6 mm in diameter respectively. ImageJ software was used to measure the size of the molten wax drops impacting the bath captured using the high speed camera. The drop was extruded through the needle and detached under its own weight without forming a thread. The molten wax drop was assumed to be homogenous without any phase change before the impact. Temperature controlled sleeves were used to control the syringe temperature, with the syringe filled with wax and varied from 40 – 75 ºC in increments of 5 ºC. The lower temperature range was chosen just

below the phase transition temperature. Above 75 °C there was no significant change in the viscosity of molten wax. An aqueous bath was placed beneath the syringe tip in a circular glass beaker and the depth of the bath was maintained at 30 mm. Since the depth of the bath was significantly larger than the radius of the wax drop, wall effects can be neglected. The properties of the bath fluids are listed in Table 4.1. The deformation was observed using the bath fluids at two different temperatures - 23 ºC and 8 ºC. Sufficient time was allowed between two succeeding impacts to allow the surface of the liquid bath layer to re-equilibrate. The release height between the bath interface and the syringe tip was varied from 1 – 25 cm to vary the impact speed. The impact speed of the drop is lowered by the drag induced by air friction on the wax and can be calculated using Newton's second law [35]. The impact speed was calculated using the following equation which accounts for the drag and was found to vary between 0.53 - 1.81 m/s when the release height was varied between 1 – 25 cm. It was verified experimentally from high speed videos.

$$U_o = \sqrt{\frac{g(1- e^{-2Ah})}{A}} \tag{4.5}$$

$$A = \frac{3C_f \rho_{air}}{\rho_{drop} R_o} \tag{4.6}$$

The term U_o denotes the impact speed, g is the acceleration due to gravity, h is the release height, C_f (friction coefficient) = 0.7796, ρ_{air} is density of air, ρ_{drop} and R_o are the density radius of the molten wax drop.

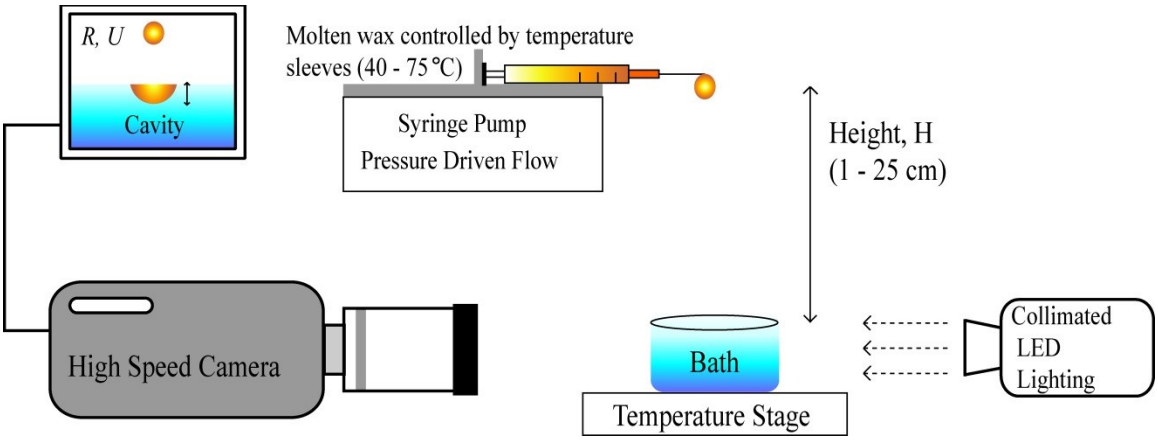

Figure 4.2. Experimental set up

4.3 Results

4.3.1 Drop Impact

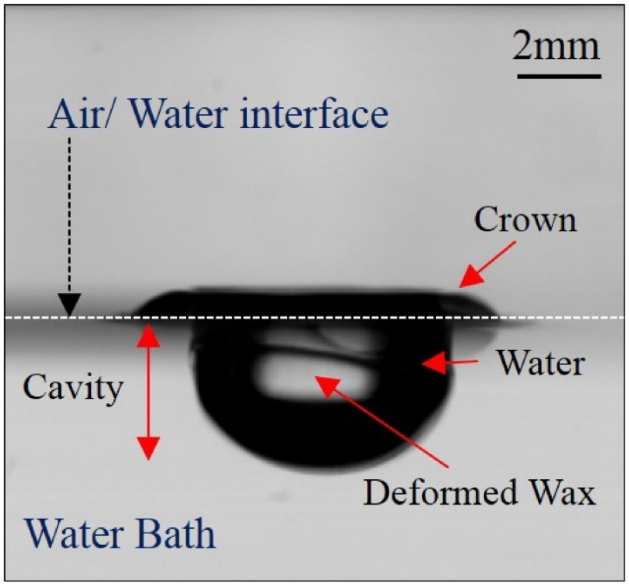

Figure 4.3. A side view image of a molten wax drop deformation at the air-water interface creating a cavity within the water bath. The dark liquid is the water bath deforming along with the wax.

The impact of the wax drop on the air-water interface is a complex phenomenon. Immediately after impact of the drop, splashing without the formation of secondary droplets occurred, the impinging drop broke the target surface and deformed. Based on the high speed imaging, we broke down the deformation process into six regions: outflow of the molten wax into the bath, cavity formation, inflow of the molten wax and bath fluid back to the original air-bath surface, jetting of bath fluid and wax into the air, outflow of bath fluid and wax to the air-bath interface and relaxation of wax leading to the solidified particle.

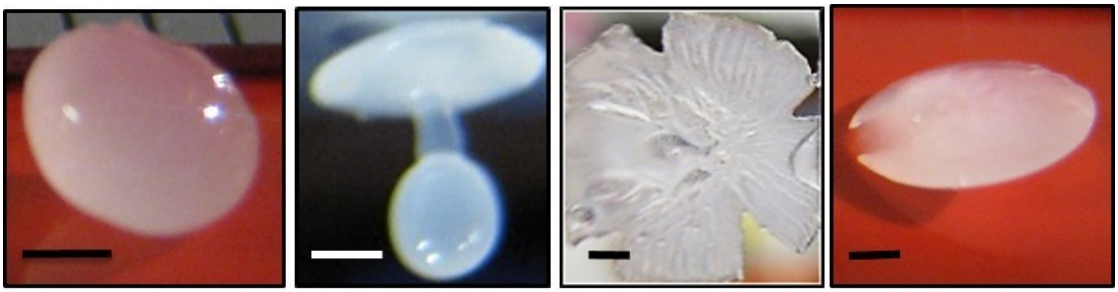

Figure 4.4. Molten wax drops deform at the interface of a water bath into four shapes - ellipsoid, mushroom, spherulite and disc. The scale bar is 1 mm.

Upon impact the wax drop deformed and broke through the air-water. It continued to flow into the bath while deforming the air-bath interface along with it. This was the "outflow region" of the molten wax drop in the water bath. A "cavity" formed in the aqueous bath while the drop deformed and lined the walls of the crater. At the circumference of the cavity a liquid sheet, crown, may rise above the original flat interface of the target bath liquid. The cavity expanded and reached a maximum at which point the wax drop reached its maximum depth from the air-bath interface (Figure 4.3). Subsequently, the cavity began to collapse. Simultaneously, the deformed wax drop attempted to retract into a minimal shape due to interfacial tension while being pushed back to the air-bath interface due to buoyancy. This was the "inflow region" and during this process, bath fluid and air interface will recover back to its initial flat shape before impact. This led to the rising of the central "Worthington jet" from the apex of the cavity [36, 37]. The jet then receded back in the "outflow region" to the air-bath interface. The wax drop relaxed in the final "relaxation region".

During the deformation of the molten wax drop, heat transfer occurred between the molten wax and the cooling bath, leading to the solidification of the molten wax drop. This is a

continuous process from when the drop impacted the bath until it reached back to the initial flat air-bath interface. There is a continuous competition between inertial, viscous, interfacial and thermal forces as the drop deformed and solidified. Dimensional analysis provides a list of relevant parameters useful in categorizing the outcomes of the molten wax drop impact.

We studied the effect of the competing forces on the deformation characteristics and the final morphology of the wax particles over a range of Weber, Capillary, Reynolds and Stefan numbers. The total time that it took for the wax drop to impact, deform and solidify in the cooling bath varied according to the wax and bath fluid properties in the range of milliseconds. We defined this time as the residence time and determined it from the high speed videos. We varied the initial temperature and viscoelasticity of the molten wax drop, drop size, impact speed, interfacial tension between the molten wax and bath fluid, viscosity and temperature of the bath. While molten wax drops impacting a solid substrate can produce only limited shapes such as lens shapes particles [38], using our liquid-liquid impact procedure with temperature variations can yield four distinct particle shapes by manipulating the process conditions - *ellipsoid, mushroom, spherulite* and *disc* (Figure 4.4). The images in Figure 4.5 were captured from various processing conditions of molten wax drops impacting a pure water bath leading to the various morphologies.

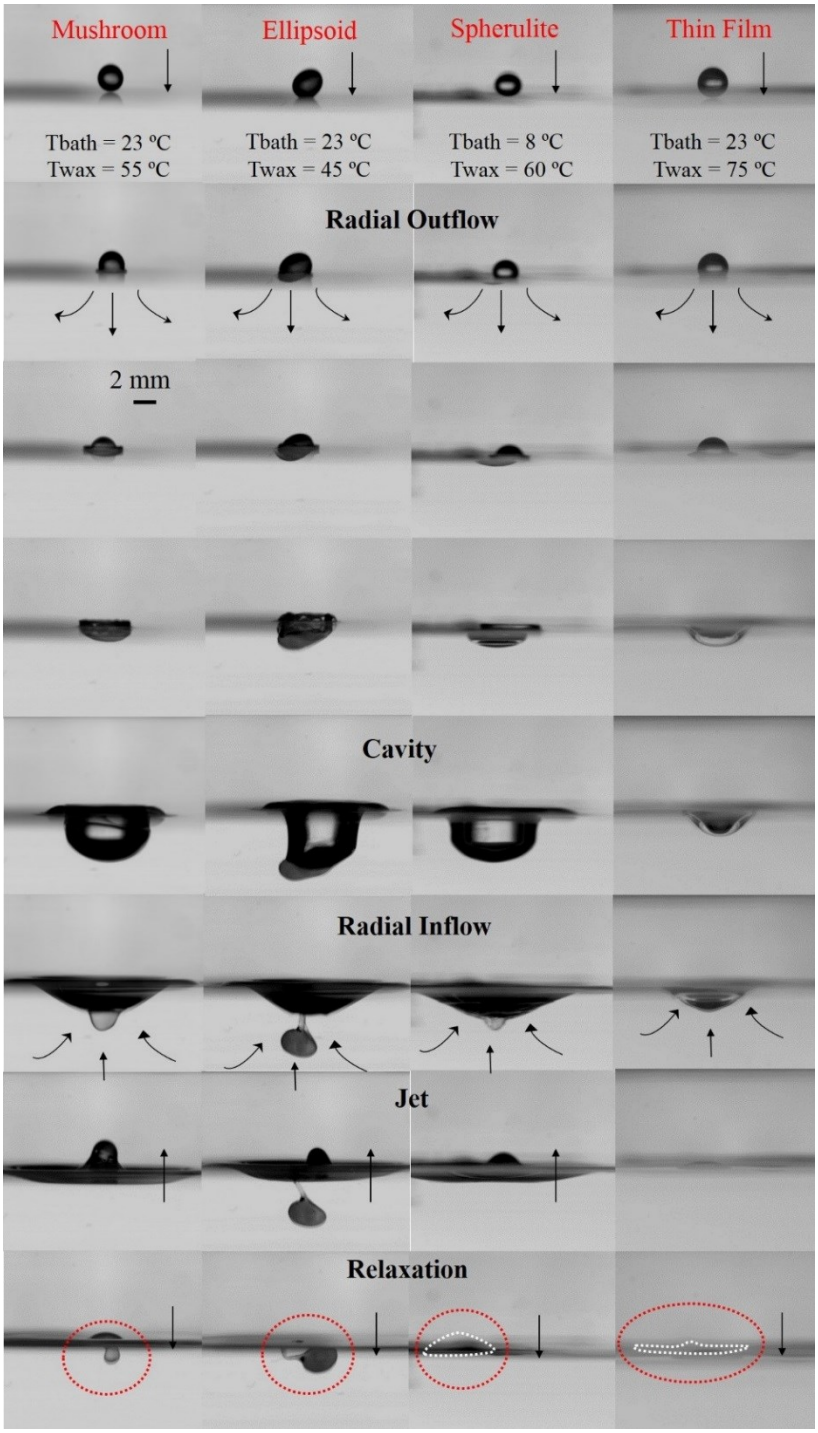

Figure 4.5. Molten wax drops deform at the interface of a water bath into four shapes at different process conditions. The time progression of the deformation for each shape is from top to bottom.

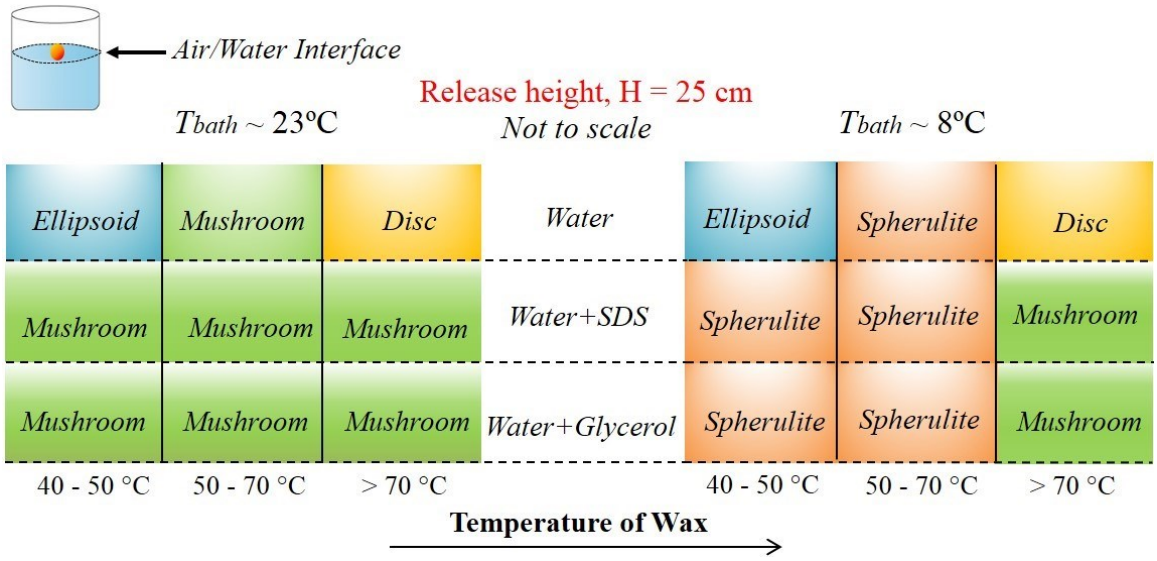

Figure 4.6. Varying particle shapes obtained under different process conditions when the wax drop is released from a height of 25 cm are shown. We vary the temperature of wax along the horizontal axis, while changing the bath fluid properties along the vertical axis. Adding surfactant Sodium dodecyl sulfate (SDS) to water lowers the surface tension. Adding glycerol to water increases the shear viscosity of the bath fluid.

Figure 4.6 outlines the experimental process conditions to tune the final wax particle shape when a spherical wax drop was released from a height of 25 cm. The horizontal axis shows the temperature variation of wax between 40 - 75 ºC. The vertical axis shows three different bath fluids arranged with increasing viscosity and density from top to bottom. The surface tension of the bath was lowered by the addition of the surfactant, Sodium dodecyl sulfate (SDS), and the bath shear viscosity was increased by the addition of 30% w/w Glycerol. Similarly, by varying the release height, the impact speed can be modified. The three bath fluids were at two temperatures, 23 ºC and 8 ºC.

Ellipsoid shaped particles were only formed at wax temperatures ranging from 40 ºC to 50 ºC where the phase transition temperature is initiated approximately at 45.93 °C. In this temperature range, the viscosity of wax was two to three orders of magnitude higher than those of the aqueous bath fluids. The deformation of the wax drop was much lower when compared with the other morphologies due its high viscosity (Figure 4.5). *Ellipsoids* can be generated using aqueous baths at 23 ºC as well as 8 ºC.

Mushroom shaped wax particles were generated with an initial molten wax temperature ranging from 40 ºC to 75 ºC depending on the bath fluid properties. The images of the *mushroom* deformation in Figure 4.6 are those in a plain water bath. Upon impact, the molten wax drop deformed and retracted back during inflow. As determined from the high speed videos, the deformed wax drop was observed to change phase in the inflow-jet region leading to the final *mushroom* morphology.

Spherulite shaped particles were only generated in lower temperature aqueous baths at 8 ºC. The initial temperature of molten wax ranged from 50 ºC to 70 ºC. The molten wax was observed to change phase in the outflow region. In the outflow region, the molten wax simultaneously deformed and solidified from the wax-bath interface to the center of the molten wax drop, causing fingering instability, which induced the *spherulite* formation.

Disc shaped wax particles were formed at a higher initial temperature of molten wax of 75 ºC. The viscosity of molten wax at 75 ºC is either comparable or one order of magnitude higher than that of the aqueous bath. Discs were generated at the lowest impact speed, 0.53 m/s, in both water containing SDS and water containing glycerol. In the case of plain water bath, *disc* shaped particles were also generated at higher impact speeds (Figure 4.6). There was higher drag

on molten wax at 75 °C in both bath fluids during the deformation of the molten wax drop after impact as compared to other morphologies leading to a shallow cavity. As a result, there was no crown or jet formation (Figure 4.5). *Discs* can be generated using aqueous baths at 23 ºC as well as 8 ºC. As determined from the high speed videos, *discs* were observed to undergo phase transition in the relaxation region.

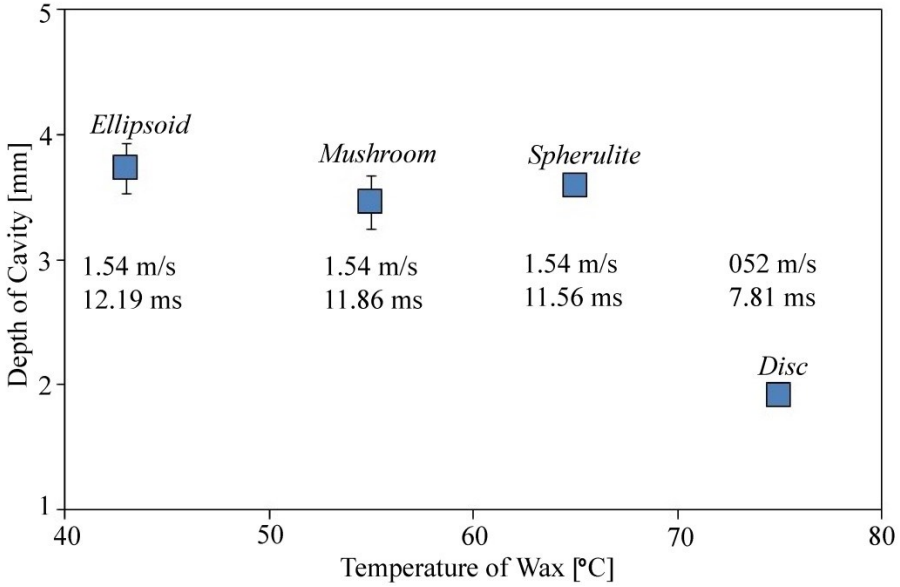

Figure 4.7. Molten wax drops deform at the interface of a water bath into four shapes at different process conditions. The impact speed and time taken for the wax drop to reach the maximum cavity depth are listed under each shape. The time required for the disc to reach the maximum cavity depth is the lowest due it to the lower impact speed.

4.3.2 Energy Analysis

The final morphologies of the wax particles were governed by delicate balances among viscous, inertial, interfacial and thermal forces. Figure 4.7 shows the particle shapes as functions of the depth of the cavity and the temperature of the wax drop extruded at 2 s^{-1} shear rate into

plain water bath at different impact speeds. We observed a similar trend with other shear rates. The impact speed, final particle shape, initial temperature of wax and the time taken to reach the maximum cavity depth are listed for each data point in the plot. As determined by the high speed videos and from Figure 4.7, we hypothesize that the maximum depth of cavity and the rise of the Worthington jet are dependent on the initial kinetic energy which in turn affects the final morphology. For lower kinetic energies, the energy transferred to the wax drop and bath after impact was not sufficient to produce a jet, as seen in the case of the *disc* shaped particle (Figure 4.5).

We also hypothesize that the time required for the temperature at the wax-bath interface to reduce to the phase transition temperature of wax or the rate of wax solidification is also critical in determining the final morphology of the wax particles. The rate of solidification increased when the temperature difference between the molten wax and bath fluid increased as observed clearly in the *spherulite* morphology.

To check our hypothesis that the kinetic and thermal energies were key factors in determining the morphology of the wax particle, we identified key energy contributions during the impact and deformation of the molten wax drop. The kinetic energy of the molten wax drop before impact was equated to the sum of the buoyant energy of the drop, interfacial energy of wax and bath, dissipative viscous energy of the wax drop and bath, and the thermal energy due to the heat loss during solidification of wax after impact. Also, after the formation of the cavity, work was required to recover the aqueous bath surface and lift the jet above the surface. This can be written as follows.

$$E_{kinetic} = E_{buoyant} + E_{interfacial} + E_{potential} + E_{thermal} - E_{dissipated} \quad (4.7)$$

The changes in the interfacial energy of the drop before and after impact were of minor importance. Using the experimental parameters, the initial kinetic energy before impact was calculated using the experimentally measured values of radius of sphere, density of wax and impact velocity and was on the order of 10^{-5} J. The buoyant energy was calculated using the values of density of bath and molten wax, radius of sphere and was on the order of 10^{-7} J. The residual kinetic energy after impact was the potential energy which assisted in the jet formation. The thermal energy calculated using the experimentally measured values of latent heat, density and radius of wax sphere was on the order of 1 J. The excess thermal energy was dissipated into the surrounding bath fluid. Based on the energy analysis and the high speed videos, we propose that the initial kinetic energy and thermal energy both play important roles in influencing the final morphology of the molten wax drop.

4.3.3 Phase Diagrams

Dimensionless analysis is useful to characterize the drop impact outcomes and compare the relative importance of the competing forces. Dimensionless numbers such as the Stefan (St), Weber (We), capillary (Ca) and Reynolds (Re) numbers were used to map cursory phase diagrams of the resulting wax particle morphologies. The Weber number compares the relative importance of inertial forces due to the impact speed of the drop with the interfacial forces due to the interfacial tension between molten wax drop and bath. The capillary number compares the viscous force due to the viscosity of the bath and the interfacial tension force due to the

interfacial tension between the drop and the bath. The Reynolds number compares the inertial forces due to the impact speed of the drop with the viscous force due to the bath. Finally, the Stefan number compares the sensible to the latent heat of molten wax. The cursory phase diagrams map the thermal effect related to the rate of solidification against the viscous, inertial or interfacial effects. The Weber number ranged from 20 - 2000, Reynolds number from 100 - 2000, capillary number from 0.01 - 1 and Stefan number from 1 - 7.

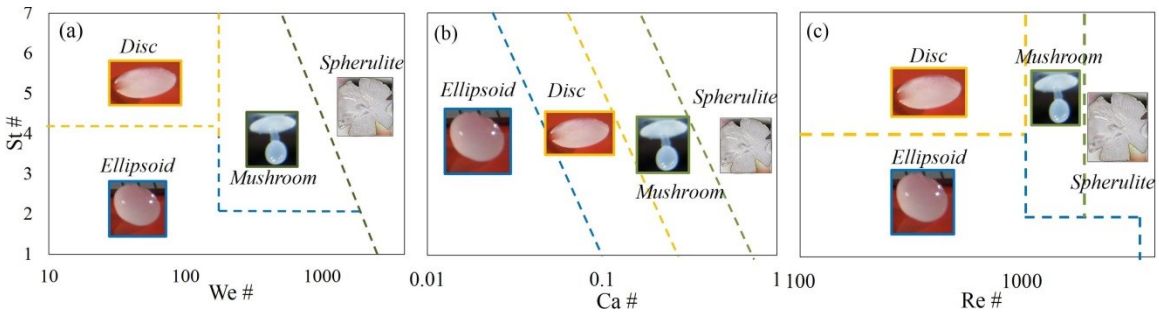

Figure 4.8. (a) Stefan number versus Weber number (b) Stefan number versus the Capillary number (c) Stefan number versus the Reynolds number.

The Stefan number was plotted against the Weber number in Figure 4.8(a). In the lower Weber number regime (We < 500), *discs* and *ellipsoids* were predominantly generated. In particular, *discs* were generated at higher Stefan numbers than *ellipsoids*. Following the initial inertial driven spreading, the residual inertia was used during the inflow and jetting regimes and influenced the dynamics of deformation. The shape evolution under the increasing Weber number demonstrated the effect of residual inertia influencing the spreading dynamics resulting in *mushrooms* and *spherulites*. In Figure 4.8b, as the viscosity of bath fluid and impact speed of wax increased or the interfacial tension decreased, the spreading of molten wax was enhanced with increasing capillary numbers. For lower capillary numbers (Ca < 0.1), *ellipsoids* were

generated followed by *discs*. As the Stefan number increased along the y-axis in the region 0.07 < Ca < 0.1, *discs* were the preferred shapes. The interfacial energy was lower for *mushrooms* and *spherulites* as indicated in the higher capillary number regime. In Figure 4.8c the horizontal axis, Reynolds number, shows increasing inertial force or decreasing viscous force. The inertial force can be controlled by varying the impact speed while the viscous force by varying the bath viscosity or wax temperature. *Mushrooms* and *spherulites* were formed at lower viscosity of wax and higher impact velocities. *Ellipsoids* were formed at higher viscosity of wax while *discs* at lower viscosity. At lower viscosity of molten wax, it deforms more and can be solidified into different shapes. These cursory phase diagrams provide a baseline for predicting the final morphologies when the initial process conditions are known. These primary observations lead us to our second objective of determining whether a correlation exists between the deformation region where phase transition occurs and the final shape of the wax particle.

4.3.4 Mathematical Modeling of the Phase Transition

When a molten wax drop impinged on an immiscible liquid surface, it underwent simultaneous deformation and solidification. A convective heat flux from the drop to the cooling medium caused the drop to freeze into a solid particle. The cooling and solidification of the molten wax drop during its movement in the cooling bath occured in two stages: (i) the temperature of the wax-water interface reaching the phase transition temperature of the wax and (ii) the subsequent propagation of the solidified phase to the core of the liquid wax drop to form a solid wax particle. Our main hypothesis was that a deformation history is produced in the drop as its temperature lowers. The final particle shape is the same as the instantaneous deformed molten

wax shape when the interfacial temperature of the molten wax-bath reduced to the phase transition temperature of wax.

Based on the above hypothesis, we propose a simplified Stefan problem for a spherical molten wax drop in a cooling bath and estimate the time required to initiate a phase transition at the interface of the molten wax and aqueous bath after impact, and correlate this time with the final shape of the wax particle. We neglect the convection inside the drop due to the high viscosity of wax and consider the cooling process of the molten wax droplet with no flow. Figure 4.9 shows a spherical wax drop of initial radius R in an aqueous medium. T_∞ denotes the temperature of the bath fluid, T_F the phase transition temperature of wax, T_s is the temperature at the interface of wax and bath while T_i denotes the initial temperature of wax.

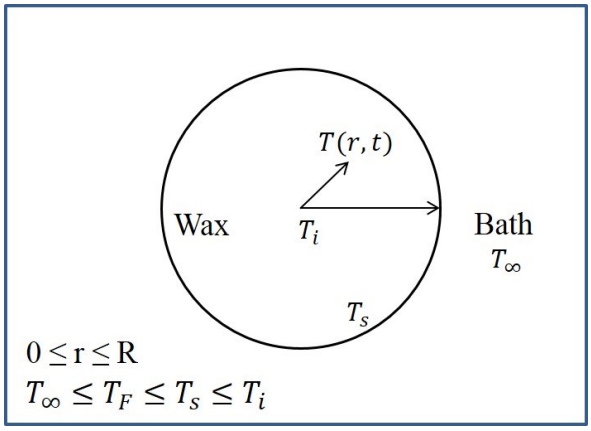

Figure 4.9. Temperature distribution in a spherical wax drop in a water bath

In the first stage where the interface of molten wax drop and bath cooled to the phase transition temperature, the temperature distribution in the spherical drop (Figure 4.9) can described by the one-dimensional heat transfer equation in spherical coordinates:

$$\frac{\partial T(r,t)}{\partial t} = \frac{\alpha}{r^2}\frac{\partial}{\partial r}\left(r^2\frac{\partial T(r,t)}{\partial t}\right); \text{ where } \alpha = \frac{k_w}{\rho_w c_p} \tag{4.8}$$

T(r,t) denotes the temperature of the wax, which is a function of position *r* and time *t*. α, k_w, ρ_w, c_p denote the thermal diffusivity, thermal conductivity, density and specific heat of wax respectively.

Initial condition is given as:

$$T(r,0) = T_i \tag{4.9}$$

Boundary conditions are employed as:

$$\frac{\partial T(r,t)}{\partial t} = 0,\ t \geq 0,\ r = 0,\ T \leq T_F \tag{4.10}$$

$$-k_w\frac{\partial T(r,t)}{\partial t} = h_f(T - T_\infty),\ r = R,\ t \geq 0 \tag{4.11}$$

The boundary condition at $r = 0$ indicates no heat flux into the center of the drop. The boundary condition at $r = R$ represents the surface energy balance, requiring the thermal energy transfer to the surface by conduction to be equal to the energy leaving the wax drop surface by convection in the bath. k_w is the thermal conductivity of the wax drop, h_f is the heat transfer coefficient for the convection between the wax drop surface and the surrounding fluid, and T_∞ is the temperature of the liquid bath. The convective heat transfer coefficient of the bath fluid, water, can be calculated and is discussed below.

We introduce dimensionless parameters,

$$\theta = \frac{T - T_\infty}{T - T_i};\ \tau = \frac{\alpha t}{R^2}, X = \frac{r}{R}$$

where θ denotes the dimensionless temperature profile relative to the initial temperature difference between the wax and the liquid bath, τ is the dimensionless time scaled by diffusivity time scale and X is the dimensionless radial coordinate scaled by the initial wax droplet radius, R. Equation 4.8 can be nondimensionalized in terms of the dimensionless parameters and reduces to

$$\frac{\partial\theta(X,\tau)}{\partial\tau} = \frac{1}{X^2}\frac{\partial}{\partial x}\left[X^2\frac{\partial\theta(X,\tau)}{\partial\tau}\right] \tag{4.12}$$

with initial condition:

$$\theta(X,0) = 1 \tag{4.13}$$

and boundary conditions:

$$\frac{\partial\theta(X,\tau)}{\partial X} = 0,\ X = 0,\ \tau \geq 0 \tag{4.14}$$

$$\frac{\partial\theta(X,\tau)}{\partial X} = -\left(-\frac{h_f R}{k_w}\right)\theta = -(Bi\theta),\ X = 1,\ \tau \geq 0,\ Bi = \frac{h_f R}{k_w} \tag{4.15}$$

where the Biot Number, *Bi*, is the ratio of the resistance to heat transfer within the wax drop to the resistance to heat transfer by convection outside the drop. The dimensionless temperature for $\theta(X,\tau)$ for heat conduction in a spherical drop can be obtained by solving the partial differential equation in Equation 4.12.

$$\theta(X,\tau) = \sum_{n=1}^{\infty}\frac{B_n}{X}\sin(\lambda_n X)e^{-\lambda_n^2\tau_F};\ 0 \leq X \leq 1,\ \ \tau \geq 1 \tag{4.16}$$

where λ_n are roots of $\lambda_n\frac{\cos\lambda_n}{\sin\lambda_n} + Bi - 1 = 0$, and $B_n = \frac{4(\sin\lambda_n - \lambda_n\cos\lambda_n)}{\lambda_n(\lambda_n - \sin\lambda_n)}$

At the interface of wax and bath at the instant of phase transition

$$\theta_F = \frac{T_F - T_\infty}{T - T_i} = \theta_F(1,\tau_F) = \sum_{n=1}^{\infty} B_n \sin\lambda_n\, e^{-\lambda_n^2\tau_F} \tag{4.17}$$

θ_F, the dimensionless phase transition temperature profile relative to the temperature difference between the initial wax and bath fluid, can be calculated from the known phase transition, initial wax and bath temperatures. Once the convective heat transfer coefficient, h_f, is estimated, the roots λ_n, can be solved. Equation 4.17 is an implicit equation for the phase transition time, τ_F, as a function of λ_n.

The convective heat transfer coefficient between the wax drop and the cooling medium depends on the relative movement and the properties of the medium. The Nusselt number, Nu, which is the ratio of convective to conductive heat transfer across a boundary, was estimated using the well-known correlation:

$$Nu = bRe^{1/2}Pr^{1/3} \tag{4.18}$$

where $Nu = \frac{h_f(2R)}{k_f}, Re = \frac{h_f U_o(2R)}{\mu_f}, Pr = \frac{C_p \mu_f}{k_f}$

The constant b is 0.69 for a sphere and 0.332 for a flat plate or disc [39]. k_f, μ_f, ρ_f, C_p denote the thermal conductivity, viscosity, density and specific heat of the fluid surrounding wax and can be measured experimentally. h_f is the convective heat transfer coefficient and is calculated from the above expressions. R and U_o denote the radius and initial impact speed of the wax drop.

For the following calculations we consider plain water as the bath fluid. From equation 4.18, the convective heat transfer coefficient can be calculated as

$$h_f = \frac{k_f b}{2R} Re^{1/2}Pr^{1/3} \tag{4.19}$$

Four experiments were conducted with the bath fluid as water and the four morphologies were obtained as a function of temperature of bath fluid, initial temperature of wax and impact speed. The processing conditions are listed in table Table 4.3.

Table 4.3. Processing conditions for the four morphologies used in the mathematical model

Experiment	T_{wax} (°C)	T_{water} (°C)	Impact Velocity (m/s)	Shape
1	40	23	1.51	Ellipsoid
2	55	23	1.51	Mushroom
3	65	8	1.51	Spherulite
4	75	8	0.53	Disc

The convective heat transfer coefficient, h_f was calculated using the relation in Equation 4.19. The value of Bi obtained by using h_f, radius R, and the thermal conductivity of wax, k_w, for each shape. Bi was found to vary only slightly from experiment to experiment. Subsequently, the nondimensional temperature at the interface, $\theta(1,\tau)$, was obtained from Equation 4.16. The phase transition initiation time, t_F, for the corresponding value of θ_F is identified from the $\theta(1,\tau)$ versus time plot. Figure 4.10a shows the variation of $\theta(1,\tau)$ with time calculated using the model for mushroom shape with an initial molten wax temperature of 55 °C, plain water bath at 23 °C and impact speed of 1.5 m/s. In Figure 4.10a, we can find the time, t_F, taken for the interface of the molten wax drop to reduce to the phase transition temperature, corresponding to θ_F on the curve. Similarly, $\theta(1,\tau)$ *vs* time was plotted for the other three shapes and t_F was found. Based on experimental data, Figure 4.10b shows the Weber number of all four wax particle morphologies in a plain water bath against the residence time of the particle in the medium for the various regions. The residence times and the times for each region were calculated from the high speed videos. The region within which the phase transition was initiated for the molten wax drop was estimated for the four shapes in plain water bath from Figure 4.10b for the calculated transition initiation time, t_F, obtained from Figure 4.10a (Table 4.4).

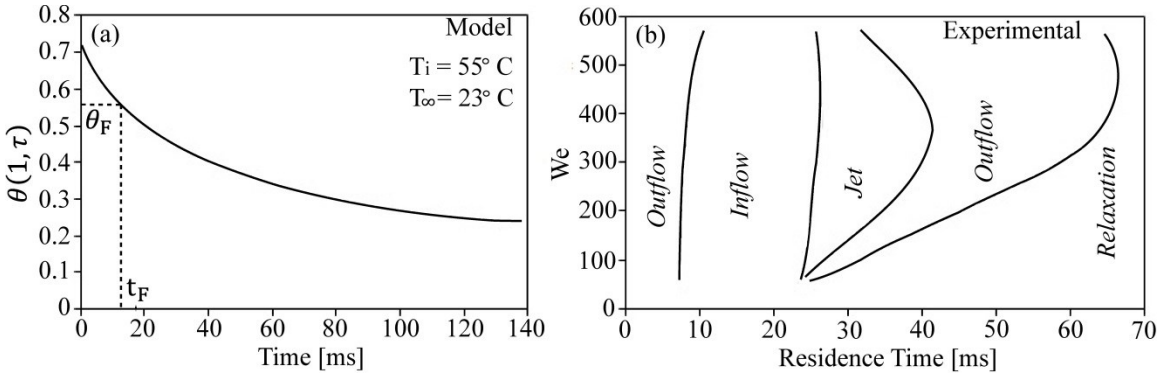

Figure 4.10. (a) The variation of phase transition deviation at the interface, θ(1,τ), with time is plotted. It is a representative plot. (b) Weber number, We, plotted against the residence times for each particle at different process conditions in a water bath.

Table 4.4. Phase transition regions for the four wax particles

Experiment	Bi	θ_F	t_F (ms) (Model)	We	Shape	Shape
1	14.58	0.78	1	567.45	Impact/ Outflow	Ellipsoid
2	14.78	0.55	15.3	444.59	Inflow	Mushroom
3	13.73	0.56	7.9	349.07	Outflow	Spherulite
4	10.35	0.35	160	53.47	Relaxation	Disc

The simplified Stefan model estimates the time taken to initiate phase transition at the interface of the molten wax and water after impact. For the *mushroom* shape, phase transition at the interface of wax and water initiated in the inflow region, *disc* in the relaxation region, *spherulite* in the outflow region and *ellipsoid* immediately after impact. The model can be extended to the other bath fluids and can be used to predict the region where the phase transition in wax is initiated and hence the final shape of wax if the initial conditions are known.

4.4 Conclusion

With the help of high speed image analysis and a simplified Stefan model, we were able to gain insight into the deformation and solidification of millimeter size molten wax drops impacting an immiscible liquid interface. *Mushroom, ellipsoid, disc* and *spherulite* morphologies were controllably generated from molten wax drops impinging on a cooling liquid surface by varying the interfacial, inertial, viscous and thermal forces. The deformation process can be separated into six regions after impact: outflow of wax into the bath, cavity formation, inflow of wax and water back to the surface, jetting into the air, outflow to the surface and relaxation leading to the solidified particle. The rate of solidification which is dependent on the initial temperatures of wax and the cooling water bath and the impact velocity play important roles in determining the final particle shape. A simplified Stefan model for a spherical drop was solved to estimate the time taken to initiate phase transition at the interface of the molten wax and water after impact. For the *mushroom* shape, phase transition at the interface of wax and water initiated in the inflow region, *disc* in the relaxation region, *spherulite* in the outflow region and *ellipsoid* immediately after impact. We produced cursory phase diagrams for the resulting particle shapes thus developing a capability along with the mathematical model for predicting the final morphologies for known initial process conditions. In the future, the above results will be used as a standard and study the deformation of micron sized, molten wax drops using microfluidic techniques.

References

[1] M. Yoshida, K. H. Roh, J. Lahann, Biomaterials 28 (2007) 2446.

[2] M. J. Murray and M. J. Snowden, Adv Colloid Interf Sci. 54 (1995) 73.

[3] L. J. Bonderer, A. R. Studart, L. J. Gauckler, Science 319 (2008) 1069.

[4] B. Y. Shekunov, P. Chattopadhyay, H. H. Y. Tong, A. H. L. Chow, Pharm. Res. 24 (2007) 203.

[5] A. Donev, I. Cisse, D. Sachs, E. Variano, F. H. Stillinger, R. Connelly, S. Torquato, P. M. Chaikin, Science 303 (2004) 990.

[6] S. Yamamoto and T. Matsuoka, J. Chem. Phys. 100 (1994) 3317.

[7] S. Gupta, Q. L. Zhang, T. Emrick, T. P. Russell, Nano Lett. 6 (2006) 2066.

[8] D. K. Hwang, D. Dendukuri, P. S. Doyle, Lab Chip 8 (2008) 1640.

[9] T. Fujibayashi and M. Okubo, Langmuir 23 (2007) 7958.

[10] J. A. Champion, Y.K. Katare, S. Mitragotri, J. Controlled Release 121 (2007) 3.

[11] D.K. Hwang, J. Oakey, M. Toner, J. A. Arthur, K.S. Anseth, S. Lee, A. Zeiger, K.J.V. Vliet, P.S. Doyle, J. Am. Chem. Soc. 131 (2009) 4499.

[12] L. Capretto, S. Mazzitelli, C. Balestra, A. Tosi, C. Nastruzzi, Lab on a Chip 8 (2008) 617.

[13] K. Liu, H. Ding, J. Liu, Y. Chen, X. Zhao, Langmuir 22 (2006) 9453.

[14] D. Dendukuri and P. Doyle, Advanced Materials 21 (2009) 4071.

[15] E. Chan, B. Lee, P. Ravindra, D. Poncelet, J. Colloid Sci., 338 (2009) 63.

[16] Y. Hu, Q. Wang, J. Wang, J. Zhu, H. Wang, Y. Yang, Biomicrofluidics 6 (2012) 26502.

[17] D.Kannangara and H. Zhang, Colloids Surf A 280 (2006) 203.

[18] R. C. Daniel and J. Berg, Adv. Colloid Interface Sci., 126 (2006) 203.

[19] J. Kim, Int. J. Heat Fluid Flow 28 (2007) 753.

[20] A.N. Lembach, H.B Tan, I.V. Roisman, T. Gambaryan-Roisman, Y. Zhang, C. Tropea, A.L. Yarin, Langmuir 26 (2010) 9516.

[21] A.J Moss and P. Green, Aust. J. Soil Res. 21 (1983) 373.

[22] R. Bhola, S. Chandra, J. Materials Science, 34 (1999) 4883.

[23] G. Trapaga, E.F. Matthys, J.J. Valencia, and J. Szekely, Metallurgical Transactions 23B (1992) 701.

[24] S. Inada and W. J. Yang, Experimental Heat Transfer, 7 (1994) 93.

[25] S. Schiaffino and A.A. Sonin, Physics of Fluids, 9 (1997) 3172.

[26] S. D. Aziz and S. Chandra, International Journal of Heat and Mass Transfer, 43 (2000) 2841.

[27] R. G. Craig, (1985) Restorative dental materials 7th ed. St. Louis: Mosby

[28] E. Endlein and K.H Peleikis, SOFW Journal 2011.

[29] Kamble et al., 2004.

[30] R. Sridhar and S. Ramakrishna, Biomatter (2013) 3.

[31] A. B Pawar, M. Caggioni, R. W. Hartel, P. T. Spicer, Faraday Disc. 158 (2012) 341.

[32] F. R. Lupi, D. Gabriele, D. Facciolo, N. Baldino, L. Seta, B. de Cindio, Food Research International, 46 (2012) 177.

[33] R. Lapasin and S. Pricl, Rheology of industrial polysaccharides: Theory and applications (1st ed.) Glasgow: Blackie Aademic and Professional (Chapter 4).

[34] M.A. Rao. Rheology of fluid and semisolid foods - Pricinples and applications (1st ed.). Gaithersburg: Aspen Publishers (Chapter 6).

[35] S. Pregent, S. Adams, M. F. Butler, T.A. Waigh, J. Colloid Inteface Sci., 331 (2009) 163.

[36] J.M. Cheny, K. Walters, J. Non-Newtonian Fluid Mech. 86 (1999) 185.

[37] L.J. Leng, J. Fluid Mech. 427 (2001) 73.

[38] R. Li, N. Ashgriz, S. Chandra, J. R. Andrews, Surface and Coatings Technology, 202 (2008) 3960.

[39] P. W. Dittus and L. M. Boelter, Univ. Calif. Pub. Eng., 1 (1985) 443 (reprinted in Int. Comm. Heat Mass Transfer, Vol. 12, pp 3.

Chapter 5
Summary and Future Work

This thesis explored the manipulation of particles at fluid interfaces using micro and macrofluidic techniques. The aim was to develop facile and cost effective techniques for fabricating soft matter spherical and non-spherical particles for application in consumer goods and biomedical diagnostics.

The results of this study demonstrate that droplet microfluidics is a facile, one-step, cost effective approach to synthesize monodispersed polyaniline microspheres. The morphology of the polymerized PANI microspheres is fibrillar and porous in nature and can be controlled by varying the initial reaction conditions. The conductivity of the individual PANI microspheres was in the range of 10^{-5}-10^{-3} S cm^{-1}. The porous and biocompatible PANI microspheres possess great potentials in the fields of biosensing as observed in the encapsulation of glucose oxidase and glucose sensingy. The PANI particles and PANI-GOx sensor show great promise and the fabrication technique eliminates the need for tedious fabrication procedures. Our next step is to explore the use of the PANI microspheres for controlled drug release.

Using oil in water emulsion technique, high speed imaging and a simplified Stefan model, we were able to gain insight into the deformation and solidification of millimeter size molten wax drops impacting an immiscible liquid interface. *Mushroom, ellipsoid, disc* and *spherulite* morphologies were controllably generated from molten wax drops impinging on a cooling liquid surface by varying the interfacial, inertial, viscous and thermal forces. The rate of solidification which is dependent on the initial temperatures of wax and the cooling water bath

plays an important role in determining the final particle shape. A simplified Stefan model for a spherical drop was solved to estimate the time taken to initiate phase transition at the interface of the molten wax and water after impact. We produced cursory phase diagrams for the resulting particle shapes thus developing a capability along with the mathematical model for predicting the final morphologies for a given set of initial process conditions. In the future, we will use the above results as a standard and study the deformation of micron sized, molten wax drops using microfluidic techniques. After controllably generating spherical molten wax drops in the microfluidic device, they will be transported off chip and impinged on a liquid interface containing the continuous phase at a lower temperature to deform and solidify the wax particles. We will also explore mathematical modeling of the above problem. This technique holds great promise for large scale manufacturing of soft matter particles in the industry.